SCUOLA DI DOTTORATO

UNIVERSITÀ DEGLI STUDI DI MILANO-BICOCCA

Dipartimento di / Department of

Fisica G. Occhialini

Dottorato di Ricerca in / PhD program Fisica e Astronomia Ciclo / Cycle XXXIII

Curriculum in (se presente / if it is) Fisica Subnucleare e Tecnologie Fisiche

Design of Mixed-Signal Electronic Instrumentation for Proton Sound Detectors

Cognome / Surname Vallicelli Nome / Name Elia Arturo

Matricola / Registration number 713915

Tutore / Tutor: Prof. Andrea Baschirotto

Cotutore / Co-tutor:

(se presente / if there is one)

Supervisor: Dr. Marcello De Matteis

(se presente / if there is one)

Coordinatore / Coordinator: Prof.ssa Marta Calvi

ANNO ACCADEMICO / ACADEMIC YEAR 2019/2020

Abstract

Acoustic proton range experimental verification technique (iono-acoustics) is based on sensing the weak thermoacoustic signal emitted by the fast energy deposition (and/or the heating process) at the end of the beam range (Bragg Peak). In this context, this thesis presents the main characteristics of the micro-electronics instrumentation used for proton sound detectors introducing specific design techniques strongly oriented to both maximization of the acoustic Signal-to-Noise-Ratio (at the Acoustic Sensor level) and Noise-Figure minimization (at analog amplifier level).

The first part of this thesis addresses all the instrumentation challenges related to iono-acoustic experiments providing specific technical details regarding both acoustic sensor design (i.e. how to build the sensor while maximizing the SNR) and the LNA design.

The experimental results of a first experiment carried out at Maier-Leibniz Laboratory in Garching, Munich, with a proton beam at 20 MeV (sub-clinical energy) will be presented and it will be shown how a dedicated mixed-signal electronics design allows to significantly improve the signal-to-noise ratio and the accuracy of the BP localization by 6 dB.

In this context, this first detector development achieves two important objectives: the improvement of the acoustic SNR and a strong simplification of the detector instrumentation w.r.t. state-of-the-art, enabling increasing accuracy of the acoustic pulse measurement, and at the same time the portability and compactness of the device.

In clinical hadron-therapy applications, variable beam energy (from 65 MeV up to 200 MeV) and variable doses are used as a function of the selected medical treatment. This induces different acoustic pulses amplitude and bandwidth, forcing advanced technological solutions capable of handling a wide spectrum of signals in terms of bandwidth, amplitude, and noise. For this reason, the second part of this thesis proposes an efficient and innovative Matlab Model of the ionoacoustic physical phenomenon, based on englobing in a single mathematical Linear-Time-Invariant-System all energy conversion processes involved in iono-acoustics. The proposed ionoacoustics model replaces classical and complex simulation tools (used to characterize the proton induced acoustic signal) and facilitates the development of dedicated detectors.

Finally, the design of a second version of the Proton Sound Detector will be presented that introduces the concept of space-domain averaging (instead of time-domain averaging based on multiple beam shot processing for noise attenuation and thus extra-doses). This detector uses a multi-channel sensor to perform a spatial average of the acquired signals

and increase the SNR by 18 dB at the same dose compared to the classic single channel approach. This approach however requires the development of highly miniaturized electronics that cannot be implemented with off-the-shelf components on Printed Circuit Boards. The design and characterization of a multichannel analog front-end implemented on a CMOS 28 nm Application-Specified-Integrated-Circuit (ASIC) which allows to process the 64 channels of the acoustic sensor in parallel is then presented. This High-Resolution Proton Sound Detector (HR-ProSD) is completed by digital circuits implemented on Field Programmable Gate Array (FPGA) that allow to locate in real time the deposition of energy in space.

Index

1.

Ionoacoustic Proton Range Verification

Chapter Abstract - This chapter introduces the ionacoustic effect and its most interesting envisioned applications. In particular, in the field of oncological hadron therapy it is particularly promising as a tool for experimental verification of the particle beam range. Various experiments at sub-clinical and clinical energies have characterized the physical phenomenon and have shown the capability of this technique to achieve sub-mm precision, using however off-the-shelf detector components and hand-made measurements that limit the performance and practicality of this technique. This thesis work is focused on the development of dedicated ionacoustic detectors with the aim of improving localization performance and obtaining real-time digital information about the particle range.

1.1 The Ionoacoustic Effect and its Applications

The ionoacoustic effect happens when a pulsed beam of charged particles interacts with a target absorber. The fast energy deposition that occurs at the end of the particle range, in a region of the Bragg curve (shown in *Figure 1.1 left* for a 200 MeV protons beam) called the Bragg Peak (BP), causes an increase in temperature and a pressure spike that propagates in the absorber medium as an acoustic wave. This acoustic wave can be sensed by acoustic sensors (AS) and can be used to obtain information about the particle beam, such as BP location, beam range, deposited dose and energy deposition profile. This so-called ionoacoustic technique has many useful applications in different fields. By providing information about the most important beam characteristics, it is a useful tool for beam characterization at accelerator facilities. Requiring just an energy absorber (usually a water tank), AS and electronics, ionoacoustic detectors are relatively simple and cheap and are characterized by limited harness compared to other nuclear imaging techniques. Besides from general beam characterization, the most interesting application of the ionoacoustic technique is in the field of hadron therapy. This oncological treatment utilizes beams of protons or carbon ions to selectively damage the tumoral tissues, exploiting the Bragg curve to deliver most of the dose to the treatment volume (i.e. where the tumor is located) while sparing the surrounding healthy tissues. By modulating the beam energy, the BP location is shifted to different depths inside the patient to match the treatment volume location. It allows a better dose conformity (that is the ratio between the target volume and the treatment plan volume) compared to X-ray based radiotherapy and is better suited for those situations where the tumor is located near radiation-sensitive tissues or organs. *Figure 1.1 left* shows a comparison between the energy deposition profile of a 200 MeV proton beam and a generic X-ray beam. Whereas X-rays follow an exponential curve with most of the dose deposited at the absorber interface, the proton beam allows to deliver the highest dose at the BP location. However, this high selectivity of the dose deposition requires a precise aiming of the beam to accurately deliver the radiation dose.

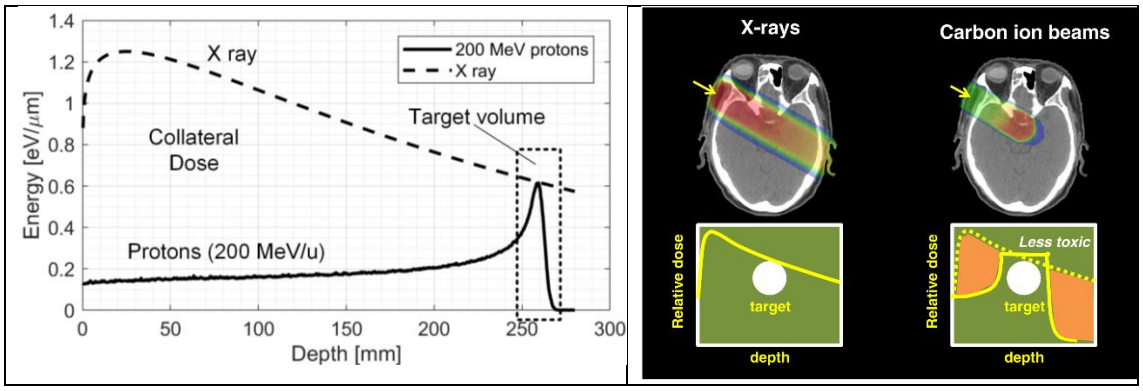

Figure 1.1 – Dose distribution of protons and X-ray irradiation simulated in water (left) and comparison between radiotherapy and hadron therapy dose deposition treatment planning (right) [1]

To improve the efficacy of hadron therapy treatments and to reduce the risk of collateral damages to healthy tissues and/or sparing tumoral tissues, a precise tool to localize the BP inside the absorber and reconstruct the dose deposition profile is then needed. Currently, nuclear imaging techniques such as Positron Emission Tomography (PET) and prompt gamma ray imaging are used at clinical facilities to calibrate the beam with phantoms before treatments and to monitor the treatment performance. These techniques are well-established and characterized but require expensive and bulky instrumentation. Their precision is also intrinsically limited to few mm. In comparison, the ionoacoustic technique has shown significantly higher precision of tens of micrometers in pre-clinical scenarios and in the mm range in clinical scenarios. Moreover, it is intrinsically real-time and thus could open the possibility of real-time beam localization (< 1 ms BP localization latency after every beam shot, determined by the acoustic wave time-of-flight and signal processing) and adaptive particle beam steering to adjust to unwanted patient movements (e.g. breathing, heart beating). The ionoacoustic technique is not meant to substitute nuclear imaging techniques due to some intrinsic limitations related to the acoustic wave propagation inside an inhomogeneous medium. For example, acoustic waves are reflected when they encounter tissues with different acoustic properties, which occurs at the interface between soft tissues and bones or air-filled cavities (e.g. lungs, intestine). As a general rule, the ionoacoustic technique is suitable for applications when treating organs that can be observed by medical ultrasound, since both techniques require acoustic waves to travel between the organ and the detector on the skin surface. However, the ionoacoustic technique high precision, low detector cost and real-time capabilities are promising to improve hadron therapy efficacy in clinical scenarios. Whereas nuclear imaging instrumentations are mature and well developed, ionoacoustic instrumentation is at an early stage and therefore it faces several performance limitations that prevent its utilization during clinical treatments. Namely, ionoacoustic experiments at clinical energies achieve millimetric precision only using very high doses, not compatible with clinical treatments. Being a relatively newly investigated phenomenon (most literature is after Sulak el al. work in 1979 and Hayakawa et al. in 1995), most ionoacoustic experiments in literature focus on the observation and characterization of the physical phenomenon with little interest in the detector improvement. This results in poor detector performances that allow to clearly observe only very intense beams (i.e. with high dose deposited per beam shot) or require heavy post-processing in the case of low dose depositions.

However, since the ionoacoustic effect is now well characterized, the natural trend in this field is to improve the technology and performance of ionoacoustic detectors to enable the application of the ionoacoustic technique as a beam characterization tool. For these reasons, this work is focused on the design and characterization of dedicated ionoacoustic detectors to improve the ionoacoustic technique performances and show that by a careful detector design it is possible to overcome the current technological limitations and significantly improve the ionoacoustic localization performances. This is a first step when

moving towards clinical scenarios, where the fast localization of high-energy low-dose beams is necessary.

1.2. State of the Art in Ionoacoustics and Thesis Motivations

Table 1.1 - Ionoacoustic State of The Art Experiments

	Assmann et al, 2015 [4]	**Patch et al, 2016 [5]**	**Hayakawa et al, 1995 [3]**	**Jones et al, 2016 [6]**	**Lehrack et al., 2017 [7]**
Beam Type	Protons	Protons	Protons	Protons	Protons
Beam Energy	20 MeV	49 MeV	100 MeV	190 MeV	220 MeV
Absorber	Water tank	Water tank, inhomogeneous target	Hepatic cancer patient	Water tank	Water tank
Particle Range	4.1 mm	21 mm	70 mm	238 mm	320 mm
Beam Diameter (FWHM of spot size at BP)	1.6 mm	4 mm	n.a.	22 mm	7.5 mm at water tank entrace
Particles/shot	10^6	$19 \cdot 10^6$	n.a.	$56 \cdot 10^6$	
Dose/shot	1.6 Gy	2 Gy	3 mGy	34 mGy	10 mGy
dP at Bragg Peak	250 Pa	200 Pa	n.a.	~ 6 Pa	~ 1 Pa
BP-Sensor Distance	25.4 mm	6.5 mm	120 mm	50 mm	75 mm
dP at sensor	n.a.	n.a.	500 mPa	32 mPa	8 mPa
Signal frequency	2 MHz	700 kHz	170 kHz	45 kHz	< 50 kHz
Detector	1 channel PZT, 3.5 MHz resonant frequency	94-ch PZT ultrasound array, 1-4 MHz pass-band	10 uV/Pa hydrophone	Commercial omnidirectional hydrophone	Commercial hydrophone
Analog Front-end	General purpose 60 dB, 10 MHz BW LNA	Medical ultrasound array	80 dB gain LNA and passive RC low-pass filter	Commercial charge amplifier	Commercial low-noise amplifier
N shots	16	1024	100-700	200	1000
Precision	45 μm	n.a.	n.a.	2.2 mm	1 mm
Accuracy	< 100 μm	1.2 mm	2 mm	4.5 mm	
Total Dose	25.6 Gy	2 kGy	300 mGy – 2.1 Gy	2 Gy	10 Gy

The ionoacoustic effect is well established and characterized by numerous works with pre-clinical and clinical protons and heavy ions both from a theoretical and experimental point of view. However, since the focus of this thesis is to characterize and improve ionoacoustic detectors, this section will analyze the current literature with a particular interest in the technological aspects in terms of detectors type and detection performances. *Table 1.1* summarizes the characteristics and measurement results of the most relevant ionoacoustic experiments performed at proton accelerator facilities. These experiments can be divided in two main sections, which are pre-clinical (< 65 MeV) and clinical scenarios (65 - 200 MeV).

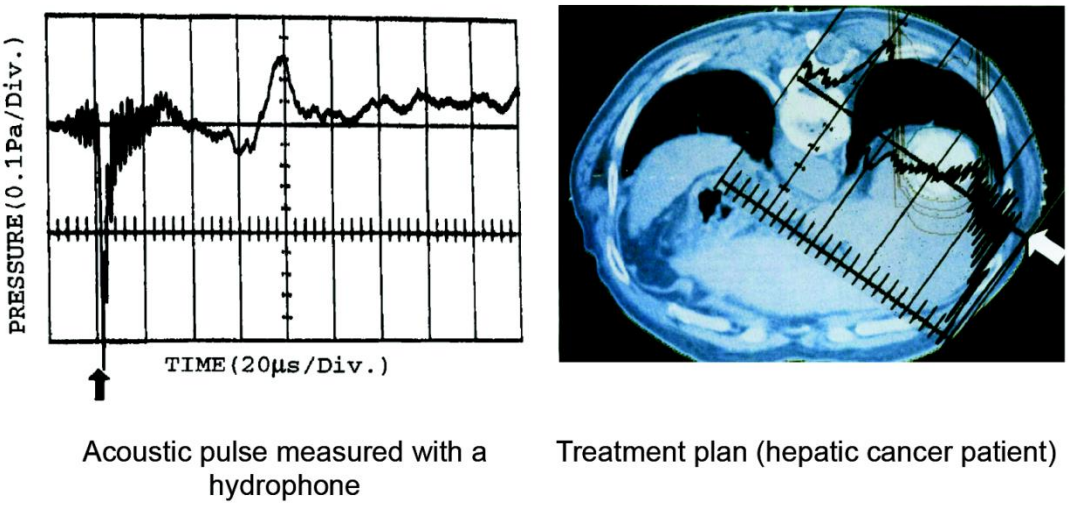

Figure 1.2 – Ionoacoustic pulse acquired during an hepatic cancer treatment superimposed with a TC scan of the patient to highlight the acoustic source location (Hayakawa et al., [3])

Pre-clinical scenarios (Assmann et al., Patch et al.) are characterized by high dose depositions (~ 1 Gy/shot) and a consequent high pressure value (~ 200 Pa) at the BP and at the sensor surface.

Assmann et al. achieves 45 μm precision and a better than 100 μm accuracy w.r.t. Geant4 simulations when performing multiple beam shots averaging to reduce the noise power and to increase the Signal-to-Noise Ratio (SNR). However, the reported 16-fold average precision is linked to a 16-fold dose deposition increase. Since each beam shot delivers 1.6 Gy at the BP, the total dose is 25.6 Gy, higher than clinical limits. Assmann et al. utilizes a commercial piezoelectric sensor (Olympus Videoscan), a general purpose Low-Noise Amplifier and an oscilloscope to acquire the ionoacoustic signal. However, few aspects that limit the resulting SNR can be observed, that are the large LNA bandwidth (10 MHz) compared to the signal bandwidth (2 MHz) and the mismatch between the acoustic sensors resonant frequency (3.5 MHz and 10 MHz) and the signal frequency. Such issues cause respectively an increase of out-of-band noise power (+7 dB) that lowers the localization precision and a loss of sensor sensitivity (-6 dB) that in turns lowers the resulting SNR (-13 dB) and, again, the localization precision. Chapter 2 will show how an improvement of such aspects leads to an improvement in BP localization precision in the same experimental conditions.

Patch et al. utilizes a medical ultrasound machine with a 94-channels probe to acquire the signal from a 50 MeV beam. The medical ultrasound machine allows to obtain a 2D acoustic image and thus a 2D localization of the BP in both a water absorber and in some silicon targets mimicking various organs. However, the lack of a proper analog front-end capable of acquiring the weaker ionoacoustic signals (compared to normal ultrasonography echoes signals) results in a massive utilization of averaging that increments the total dose to 1 kGy.

When considering experiments performed at clinical energies, they are characterized by lower dose depositions at the BP, in the order of few tens of mGy per beam shot. This results in a pressure generation at the BP which is around two orders of magnitude lower than in pre-clinical scenarios, thus defining clinical scenarios as critical in terms of clear signal acquisition.

In 1995, Hayakawa pioneer work showed that a clear acoustic signal was observable in an epatic cancer patient treated with 100 MeV protons using a commercial hydrophone. The acoustic signal (showed in *Figure 1.2*) allowed to localize the BP inside the patient with 2 mm accuracy. However, averaging was again needed to observe such signal, and Hayakawa reports 100-700 averaging with 3 mGy dose deposition/shot. This result is very interesting since it shows that ionoacoustic signals can be observed also in inhomogeneous tissues within a patient.

More recently, Jones et al. and Lehrack et al. conducted experiments at with 190-220 MeV proton beams, achieving sub-mm precision in water phantoms but again after averaging 100-1000 beams shots. These experiments utilize commercial hydrophones (i.e. *Cetacean Research C305X, Seattle, USA*) and general-purpose electronics and heavily relies on averaging to visualize the ionoacoustic signal, using a total dose of few Gy. Jones et al. introduces also a deconvolution technique to compensate for unwanted effects caused by long accelerator pulse time and thus reduce systematic errors in the measurement and improve accuracy with non-ideal beam characteristics.

In conclusion, the vast majority of experiments use off-the-shelf general-purpose sensors, electronics, oscilloscopes and hand-made measurements and focus on characterizing the physical phenomenon, with little interest in detector improvement. This results in poor measurement performances that are addressed by heavily relying on post-processing algorithms (i.e. averaging). This however limits the capability of the ionoacoustic technique when applied to the weakest beams and clinical scenarios.

However, to improve this technique it is necessary to move towards the use of a compact and dedicated instrumentation. This thesis work has been done within the Proton Sound Detector (ProSD) project funded by the Italian Institute for Nuclear Physics (INFN). The ProSD project goal is to design dedicated ionacoustic detectors that improve measurement results by pursuing two technical advancements:

- the use of a dedicated system that allows to acquire ionoacoustic signals with low-noise, thus improving the Bragg peak localization precision;
- the implementation of a compact, portable and automated detector that allows to obtain digital data on the measurement in real-time, thus effectively achieving a proton-to-bit conversion.

This thesis will work in this direction and in particular will focus on a specific pre-clinical experimental setup (20 MeV protons) to show that the detector performance can be significantly improved by the use of a dedicated instrumentation.

1.3. Thesis Outline

This thesis is organized as follows. In Chapter 2 the main characteristics of the ionoacoustic effect and ionoacoustic experiments are explained while presenting the results of a beam test performed with a 20 MeV proton beam. Along with the main characteristics of the ionoacoustic effect, a preliminary dedicated ionoacoustic detector, called Proton Sound Detector (ProSD) will be described. The ProSD performances will be compared with state of the art to show how a dedicated approach allows to improve the BP localization precision for the same dose, or to lower the dose necessary to achieve a given precision.

Chapter 3 will present a model of the ionoacoustic effect as a Linear Time-Invariant system (LTI). It will be shown how this simple model allows to obtain an accurate simulation of the ionoacoustic signal and therefore allows to obtain in a simple and fast way the information necessary for the design of a detector. This model will be used to investigate which are the properties of the particle beam that maximize the amplitude of the ionacoustic signal. Finally, a comparison will be made between pre-clinical scenarios and clinical scenarios in terms of signal amplitude and signal-to-noise ratio.

Chapter 4 will show how to avoid the use of time domain averaging to improve the signal to noise ratio, moving to the use of space domain averaging performed through multi-channel acoustic sensors. This approach allows to increase the SNR at the same dose but requires miniaturized electronics implemented on application-specific integrated circuits (ASIC). The design and preliminary characterization of a dedicated ASIC will then be presented, which together with a multi-channel sensor and hardware signal processing will form the so-called High-Resolution Proton Sound Detector. The purpose of HR-ProSD is to further improve the accuracy in localization at the same dose, or equivalently reduce the dose necessary to obtain a certain precision.

Finally, the obtained results will be discussed, and conclusions will be drawn.

2.

20 MeV Proton Sound Detector Design and Experimental Results

Chapter Abstract - This chapter will present the results of a preliminary beam test that has been performed at the Maier-Leibniz Laboratory in Garching, Munich. In this test, a Proton Sound Detector (ProSD) was tested, whose performance has been enhanced by a dedicated analog front-end (ProSD AFE). This chapter shows that a dedicated design of the ProSD AFE allows to improve the overall detector performances by 6 dB and reduce the total dose deposition to 25% compared with previous experimental results. The hereby presented ProSD, compared to state-of-the-art instrumentation, has lower harness and utilizes real-time digital signal processing to obtain an automatic and fast acquisition of the physical phenomenon. Moreover, dedicated real-time algorithms compute the Bragg peak position in real-time, effectively achieving a proton-to-bit conversion. This Chapter has been published as an invited contribution at the IEEE Transaction on Circuits and System – I with the title *"22 dB Signal-to-Noise Ratio Real-Time Proton Sound Detector for Experimental Beam Range Verification" [10]*.

2.1 20 MeV Ionoacoustic Experimental Setup

Figure 2.1 shows a picture of the 20 MeV proton beam experimental setup. A 10 MV terminal voltage accelerates protons to an energy of approximately 20 MeV per particle, which then exit from vacuum to air and enter a water phantom after passing a Kapton entrance foil. The beam is pulsed by means of a chopper-buncher system, featuring a pulsing frequency of 4.8 kHz and an almost rectangular pulse of 120 ns length. The BP is located at 4.1 mm from the entrance foil along the beam axis. The ionoacoustic signal generated at the BP propagates in water and is sensed by a Lead-Zirconate-Titanate (PZT) piezoelectric AS located 2.54 cm away from the BP along the beam axis. The signal is then amplified by the ProSD, whose generic block scheme is shown in *Figure 2.2*. The ionoacoustic signal is first amplified by means of a variable gain low-noise amplifier (LNA), in turn composed by two amplification stages. Then a Low-Pass Filter rejects out-of-band noise components and interferers. Finally, an ADC converts the signal in digital domain and a dedicated digital system on FPGA controls the signal acquisition and sends data to a PC graphic user interface (GUI) via USB 2.0. The GUI displays the acquired signals and performs digital signal processing (DSP) such as time of flight (ToF) measurement and signal averaging.

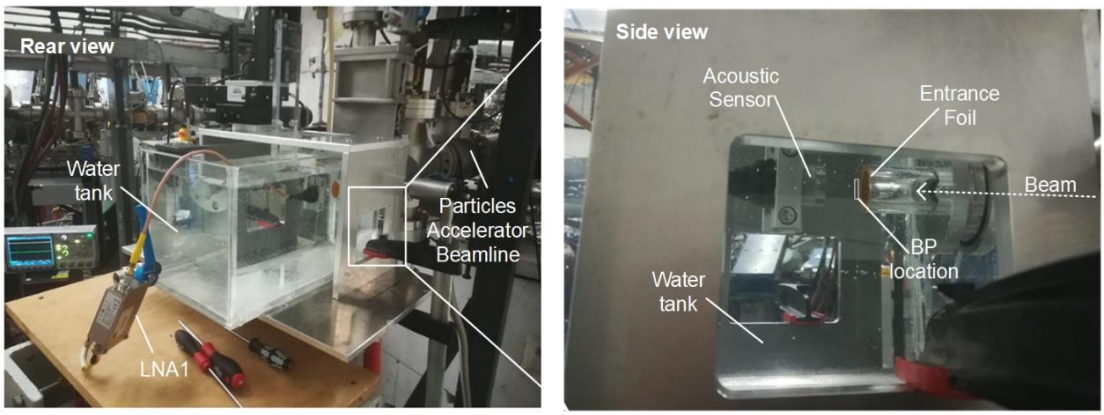

Figure 2.1– 20 MeV protons experimental setup

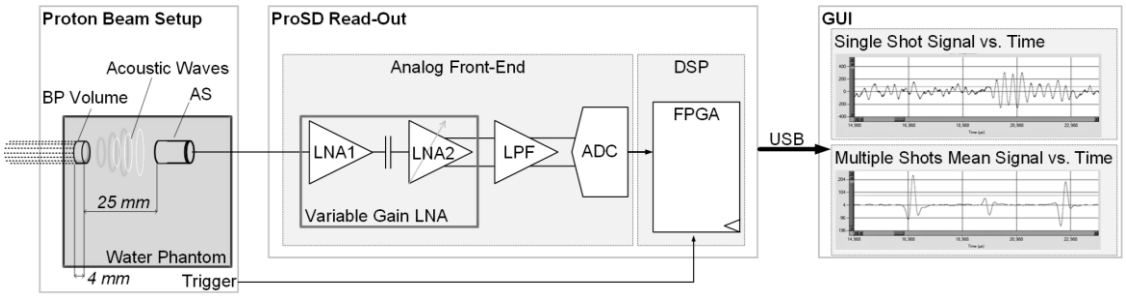

Figure 2.2– Generic block scheme of the Proton Sound Detector

2.2. Ionoacoustic Signal Generation

According to Geant4 simulations, the resulting proton range in water is 4060 μm, estimated from the water phantom entrance window to the BP position. The BP full width at half maximum (BP_{FWHM}) is 320 μm and the proton beam has a diameter of 2 mm that corresponds to height and diameter, respectively, of a BP heating region having a cylindric shape and 0.64 mm3 volume, as shown in Figure 2.3– . Such BP surrounding volume (BP_{VOLUME}) hosts a thermodynamic isochoric and adiabatic process regulated by the following equation Eq. 2.1 where V, T, P are heating region volume, temperature and pressure, respectively, k and β are the isothermal compressibility and volume expansion thermal coefficients.

$$\frac{dV}{V} = -k \cdot P + \beta \cdot T \rightarrow \Delta P = \frac{\beta}{k} \cdot \Delta T \qquad \textit{Eq. 2.1}$$

Such equation holds true when two conditions are fulfilled. First, the energy deposition has to be fast enough so that it is considered adiabatic and isocoric. The first condition is fulfilled if the energy deposition lasts less that the thermal confinement time t_{TH}., that depends on the BP_{FWHM} and the water thermal diffusivity (D_T = 0.143 mm^2/s) as shown in Eq. 2.2. In this 20 MeV scenario, the thermal confinement is equal to 0.6 s. The second condition is fulfilled if the energy is deposited within the stress confinement time T_{STRESS} (Eq. 2.3) equal to the ratio between the BP_{FWHM} and the sound speed in water (c_w = 1488 m/s). In ionoacoustic experiments, the stress confinement is usually much shorter than the thermal confinement and is equalt to 220 ns for 20 MeV protons.

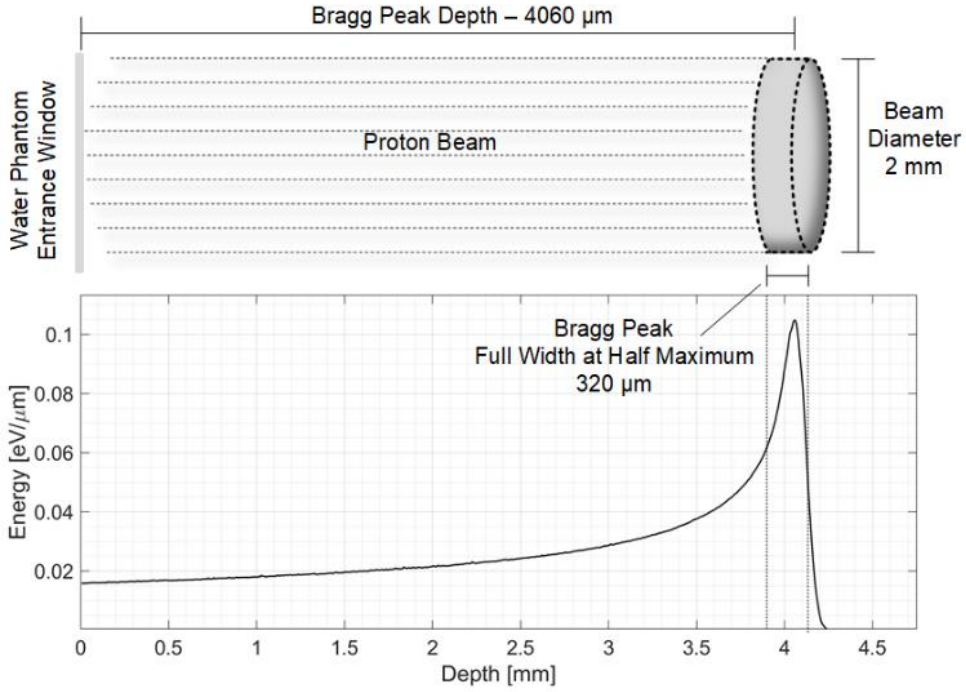

Figure 2.3– Bragg curve for 20 MeV protons and simplified equivalent cylindrical pressure source

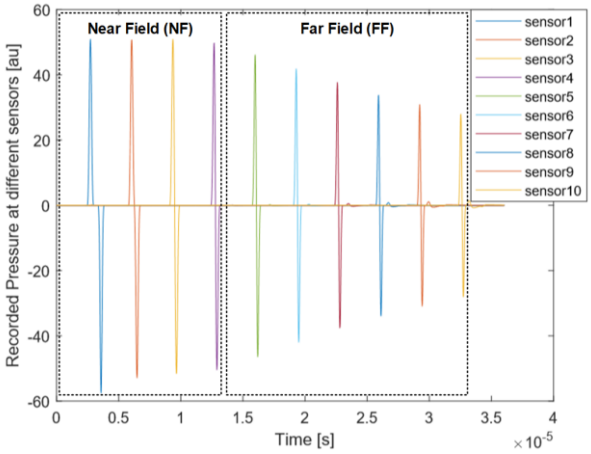

Figure 2.4– Acoustic signal amplitude at different distances within Near Field and in Far Field

$$t_{TH} \cong \frac{BP_{FWHM}^2}{D_T} \qquad \textit{Eq. 2.2}$$

$$t_{STRESS} = \frac{BP_{FWHM}}{c_w} \qquad \textit{Eq. 2.3}$$

If these conditions are met, the pressure variation at constant volume and without heat dispersion is proportional to the temperature variation (ΔT) caused by the energy deposition (E_{DEP}) at the BP volume:

$$\Delta T = \frac{E_{DEP}}{C_V \cdot (\rho \cdot BP_{VOLUME})} \cong 0.3mK \qquad \textit{Eq. 2.4}$$

where C_V is the constant volume water specific heat and BP_{MASS} is the total heated mass ($\approx \rho \cdot BP_{VOLUME}$). Finally, the pressure pulse amplitude at the BP assuming a point-like source is:

$$\Delta P_{BP} \cong \frac{\Delta T \cdot \beta}{k} = \frac{D \cdot \beta}{k \cdot C_V} \cong 80\ Pa \qquad \textit{Eq. 2.5}$$

where D is the dose deposited at the BP. Such pressure signal spherically propagates through the water phantom and then the acoustic pulse read out by the AS (positioned at 25 mm distance as shown in Figure 2.2) experiences a 24 dB (a factor 16) attenuation mainly due to the attenuation from spherical waves propagation in water in far fields conditions. As a matter of fact, the attenuation is inversely proportional to the BP-AS distance ($d_{AS\text{-}BP}$), equal to 25 mm. An estimation of this attenuation can be calculated as in formula (4) considering a disk source with a near field length $NF = D_B^2/4\lambda$, where λ is the wavelength of the acoustic wave, equal to $2 \cdot BP_{FWHM}$ or 640 µm. As a first approximation, the acoustic signal amplitude remains constant in the near field region and is attenuated as 1/d in the far field region, as shown in Figure 2.4.

$$P_{ATT} \cong 20 * log10\left(\frac{NF}{d_{AS-BP}}\right) = -24\ dB \qquad \textit{Eq. 2.6}$$

Table 2.1 – Proton Beam Input Parameters

Parameter	Symbol	Value
Particle Energy	E	20 MeV
Current Pulse Time Window	TW	120 ns
Stress confinement	t_{stress}	220 ns
Proton Bunch Number	NP	1 M
Beam Diameter	D_B	2 mm
Pulse Equivalent Injected Charge	Q_{IN}	0.16fC
Deposited Energy Dose	E_{DEP}	0.8 Gy
BP FWHM	BP_{FWHM}	0.32 mm
Beam Depth Range	R	4.060mm
BP Volume	BP_{VOLUME}	0.64 mm^3
Water Specific Heat at const. volume	C_v	4186J/(Kg·K)
Water Volume Thermal Coefficient	β	$2.14 \cdot 10^{-4}$ K^{-1}
Water Isothermal Compressibility	k	$5 \cdot 10^{-10}$ Pa^{-1}
Water Density	ρ	997 Kg/m^3
Sound Speed in Water (22.3 °C)	c_w	1492 m/s

Table 2.2 – ProSD Analog Front-End Parameters

	Parameter	Value
Acoustic Sensor	Pass-band Sensitivity	~10 µV/Pa
	Pass-band Frequency Range (- 6 dB)	2.45 – 4.95 MHz
	Capacitance	1 nF
	Output Noise Power	5.82 μV_{RMS}
	Input Referred Noise	~580 mPa_{RMS}
LNA	Pass-band Gain	60 dB-80 dB
	-3dB lower frequency	10 kHz
	-3dB upper frequency	4 MHz
	Input Referred Noise Voltage	2.25 μV_{RMS}
Low-Pass Filter	Pass-Band Gain	0 dB
	Poles Frequency	2·π·4 MHz
	Poles Quality Factor	0.707
A-to-D Converter	Sampling Frequency	80 MHz
	Number of Bits	10
	Equivalent Number of Bits (ENOB)	9.5

The average beam current has been measured with a Faraday cup and is equal to 1.33 µA, leading to around 10^6 particle per pulse. Each particle deposits 4 MeV in the BP volume, thus the total energy deposited per beam pulse is 0.6 µJ. Considering the BP volume in water, the total dose deposited per beam pulse is around 0.8 Gy at the BP and 0.26 Gy in the pre-BP volume. The main physical parameters regarding beam characteristics, BP curve and the related thermodynamics are listed in Table 2.1.

2.3. Acoustic Sensor Characteristics and ProSD Read-Out Electronics

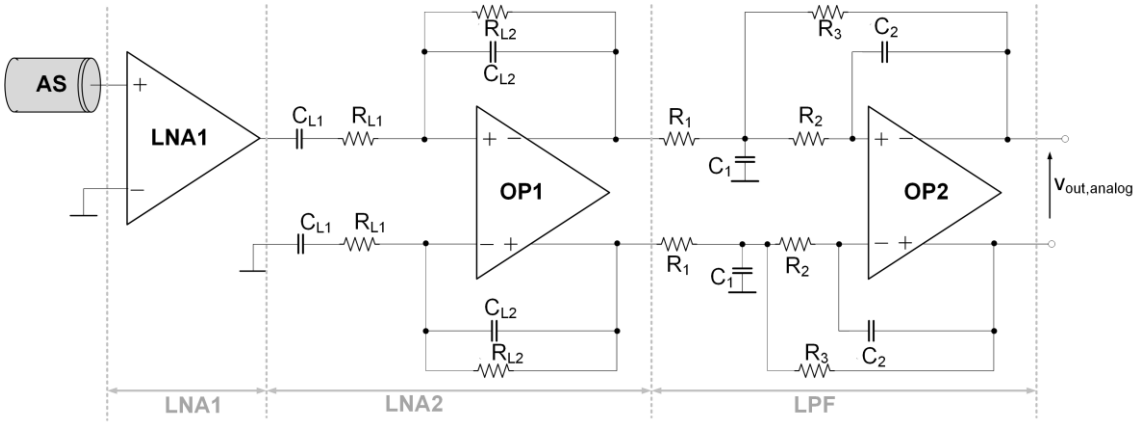

Figure 2.5– Acoustic signal amplitude at different distances within Near Field and in Far Field

The system-level parameters of the acoustic AFE, organized by stage, are listed in Table 2.2. The selected AS is a Lead-Zirconate-Titanate (PZT) piezoelectric transducer feeding a dedicated acoustic analog front-end (AFE) electronics. The AFE cascades a 0.9 nV/√Hz Low Noise Amplifier (LNA, in turn based on two ac-coupled gain stages), a 5 MHz -3 dB frequency Low-Pass Filter (LPF, for out-of-band noise rejection) and a 10b 80 MS/sec A-to-D converter. Importantly an on-board Field-Programmable-Gate-Array (Xilinx-Spartan-6 200 MHz clock frequency FPGA) real-time communicates with a server quickly measuring the beam depth referred to the entrance foil and drawing the acoustic signal in both time and frequency domains through an easy-to-use Graphic User Interface (GUI). The LNA is composed by the cascade of two gain stages:

- LNA1 is responsible for noise and 60 dB amplification that makes negligible the noise power contribution from the following stages;
- LNA2 has then more relaxed noise requirements and thus it can be optimized for performing variable gain with 0, 10 and 20 dB possible gain values.

Dividing gain in two LNA stages allows meeting two key requirements for analog channel signal processing which are to minimize noise w.r.t. the AS noise floor (LNA1) and to maximize the A-to-D input Dynamic Range up to 0.5 V0-PEAK, thus enhancing the final Equivalent-Number-of-Bits. Moreover, the whole LNA acts as a rough 1st order bandpass filter by means of an input AC coupling (with 10 kHz -3dB frequency) that also reject 1st-stage voltage offset and an upper bandwidth of 4 MHz (in line with AS bandwidth). LNA bandpass frequency response mitigates three relevant issues in acoustic sensing that could corrupt the signal quality and thus may reduce the final SNR:

- reduces out-of-band noise and interferers providing channel filtering selectivity;
- rejects both offset and flicker noise;

Table 2.3 – Acoustic AFE Analog Section Parameters

	Parameter	Value
LNA1	-3 dB Frequency	10 MHz
	Pass-Band Gain	60 dB
	LNA1 IRN	0.9 nV/√Hz
LNA2	OP1,2 Unity Gain Frequency	500 MHz
	OP1,2 dc-gain	125 dB
	OP1,2 IRN	2.9 nV/√Hz
	R_{L1}	1 kΩ
	R_{L2}	10 kΩ
	C_{L1}	1.6 nF
	C_{L2}	4 pF
Low-Pass Filter	R_1, R_2, R_3	6.2 kΩ
	C_1	6.8 pF
	C_2	2.2 pF

- reduces the sensitivity of the acoustic AFE to out-of-band interferers coming from clocks (80 MHz), motor drivers and USB/digital signals.

LNA1 is a commercial low-noise amplifier and has been placed just outside the water tank, as close as possible to the acoustic sensor and away from digital signals to limit interferers. The electrical scheme of LNA2 and LPF is illustrated in Figure 2.5.

The LNA1 input referred noise (IRN) is 2.25 µVrms (over 10 kHz-4 MHz bandwidth). LNA2 acts also as a single-ended to fully-differential converter increasing power-supply and common-mode rejection ratio. The LNA drives a 4 MHz -3 dB low-pass filter that further reduces high frequency noise. The LPF synthesizes a 2nd-order transfer function adopting a Rauch topology. The synthesized complex-conjugate poles have 0.707 quality factor. For noise minimization and mask fitting, resistors (R_1, R_2, R_3) and capacitors (C_1, C_2) are sized as a function of noise and transfer function specifications as follows:

$$R_1 = \frac{IRN_{LPF}^2 - \left((1 + 1/G) \cdot IRN_{OP1}\right)^2}{8 \cdot k \cdot T \cdot (1 + 1/G) \cdot (2 + 1/G)}$$

$$R_3 = G \cdot R_1$$

$$R_2 = R_1 \qquad \textit{Eq. 2.7}$$

$$C_1 = \frac{1}{\omega_0 \cdot Q \cdot \left(R_2 + R_3 + \frac{R_2 \cdot R_3}{R_1}\right)}$$

$$C_2 = \frac{1}{C_1 \cdot R_2 \cdot R_3 \cdot \omega_0^2}$$

where G is the pass-band gain equal to 0 dB. The LNA2 and LPF operational amplifiers (OP1 and OP2) are LTC6363 and meet the noise (2.9 nV/√Hz), gain (125 dB dc-gain) and bandwidth (500 MHz unity gain frequency) specifications. The LPF filter output signal is then converted into digital domain by a 10b SAR A-to-D converter at 80 MHz sampling frequency for an equivalent 800 Mbit/sec sample rate.

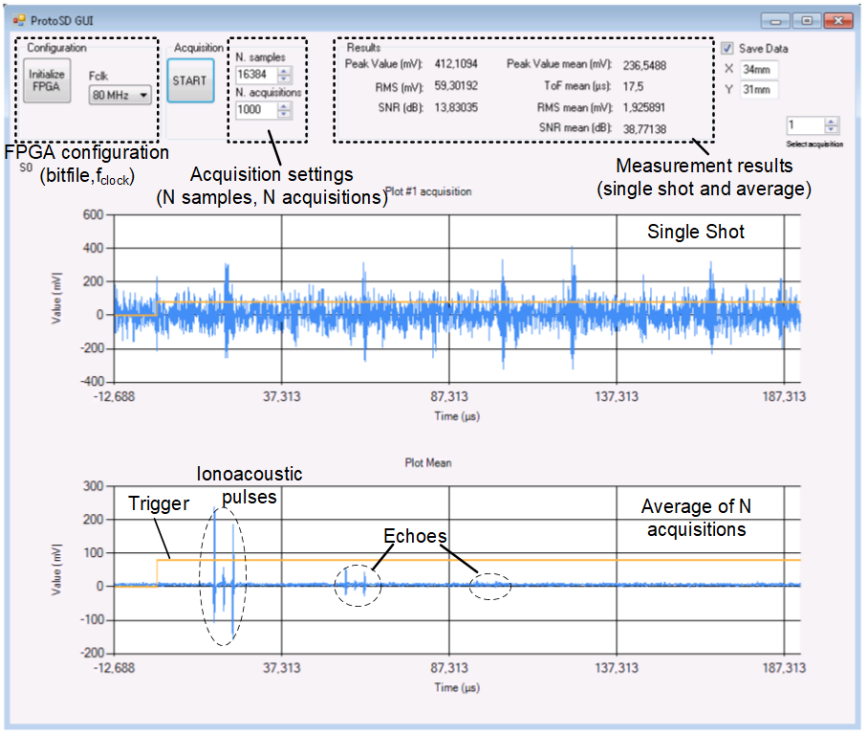

Figure 2.6– Proton Sound Detector Graphic User Interface (GUI)

The A-to-D SNR considering its ENOB of 9.5b, is 69.0 dB with 59.0 dB coming from 9.5b resolution and the remaining 10 dB from 80 MHz/(2·4 MHz) oversampling ratio. Table 2.3 reports some of the most relevant design parameters for LNA, LPF and A-to-D converter.

2.4. Digital Signal Processing

A digital 10b parallel bus connects the A-to-D converter to a Xilinx Spartan 6 FPGA mounted on an OpalKelly XEM6010 development board by means of an HPC connector. The FPGA is programmed by a dedicated VHDL-code acoustic Digital Signal Processing (DSP) that performs the following operations:

- manages the communication between the A-to-D converter and the FPGA;
- stores and plots the single realization of a single shot pressure signal vs. time and frequency;
- calculates the detected Time-of-Flight as a function of incident and reflected (pulse against the water phantom entrance wall) pressure;

reads-out and averages for Nshot times (with Nshot selected from the external GUI, Figure 2.6) the pressure signal (one signal vs. time realization for one single beam shot) rejecting noise power and thus improving the final SNR as follows:

$$SNR = SNR_{SINGLE-SHOT} + 10 \cdot \log_{10} N_{SHOTS} \qquad Eq.\ 2.8$$

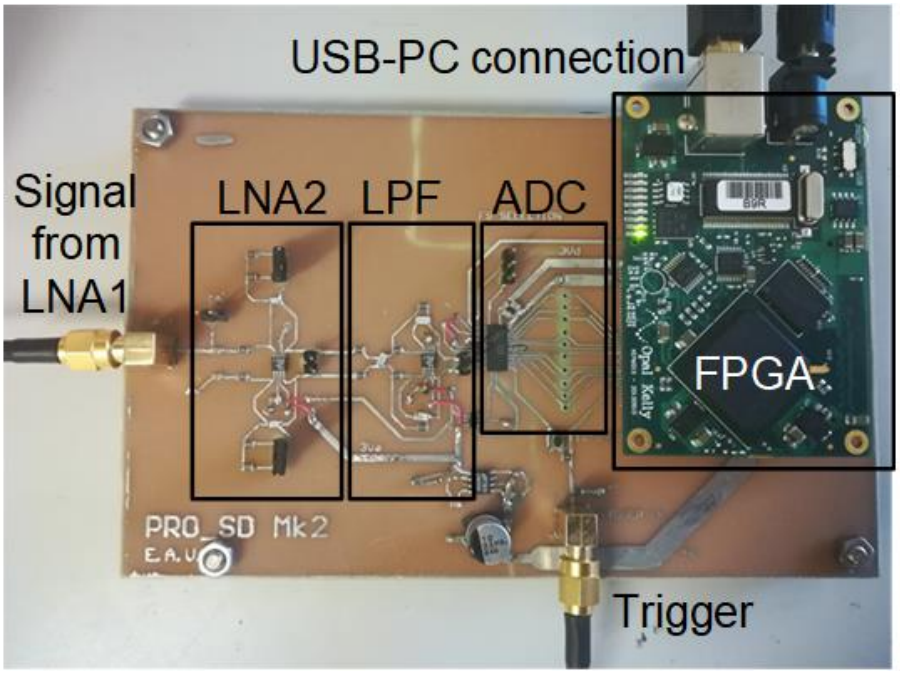

Figure 2.7– Comparison of dose distribution of protons with X-ray irradiation simulated in water

where $SNR_{SINGLE\text{-}SHOT}$ is the achieved SNR for one single shot acquisition and N_{SHOTS} is the total number of beam shots used for averaging. Notice that such averaging algorithm, which is crucial for enhancing the SNR (critically affected by the weak pressure pulse comparing with commercial AS noise power) is in this work performed in hardware domain or in real-time. The final C++ GUI is designed on a PC-server via-USB connected with the FPGA DSP.

2.5 ProSD AFE Electrical Characterization

Before characterizing the detector with proton beams and testing the device capability to detect acoustic waves accurately, the ProSD analog channel has been electrically validated. The AFE has been connected to a 5 GHz Spectrum Analyzer and signal/noise frequency-domain measurements have been carried out. ProSD AFE and DSP are mounted on a 10x16 cm^2 printed-circuit-board (PCB, whose photo is shown in Figure 2.7), SMA connected with the in-water LNA1. A 10b bus drives the A-to-D converter digital data stream towards the FPGA where the following real-time operations are executed:

- communication, i.e. data receiving from ProSD AFE;
- signal sorting vs. shot number (Nshot);
- signal plotting in time/frequency-domain;
- Time-of-Flight calculation.

A. ProSD AFE Frequency Response

The measured frequency responses of LNA, LPF and whole AFE channel are shown in Figure 2.8. LNA2 is set to maximum 20 dB gain, leading to a global AFE 80 dB gain.

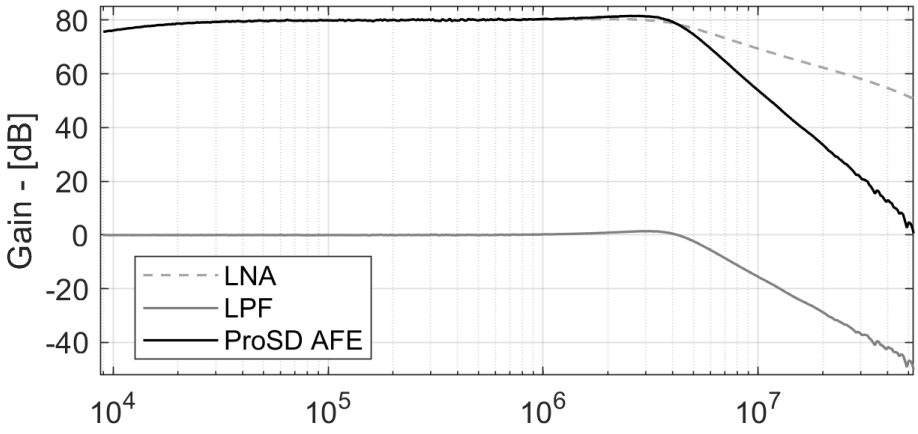

Figure 2.8– Comparison of dose distribution of protons with X-ray irradiation simulated in water

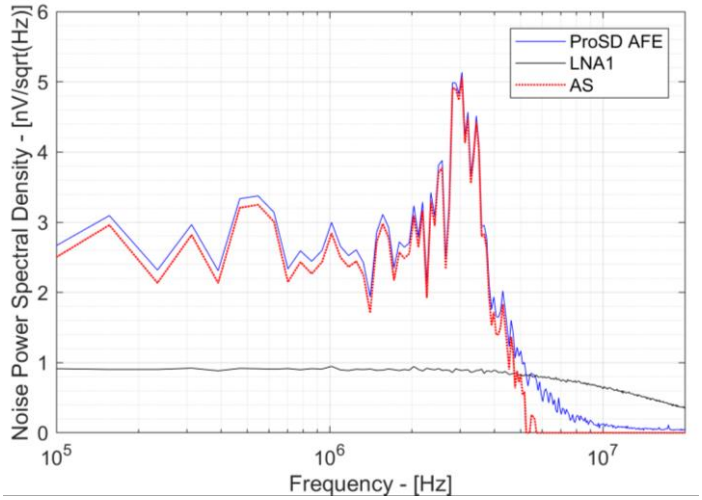

Figure 2.9– Comparison of dose distribution of protons with X-ray irradiation simulated in water

The -3 dB frequency of the ProSD AFE channel is 4 MHz (AS resonant frequency is 3/3.5 MHz) and asymptotically out-of-band falls with -60 dB/decade, (two complex conjugated poles from LPF and a single real pole from LNA2).

B. ProSD AFE Noise Spectrum

Figure 2.9 shows AFE channel noise measurement in frequency domain, where the vertical axes represents the input referred noise power spectral densities (PSD) of the main noise contributors (Acoustic Sensor and LNA1) and total ProSD AFE channel noise. In-band LNA1 noise PSD is 0.9 nV/√Hz. The AS exhibits 2.5 nV/√Hz PSD, corresponding to 5.82 µVRMS noise power. It is possible to observe a noise PSD peaking at 3.5 MHz, corresponding to the AS resonant frequency. The low noise power spectral density of LNA1, integrated over the LPF bandwidth, leads to a total input referred noise power of 2.25 µVRMS. This value, when compared to the 5.82 µVRMS AS noise power,

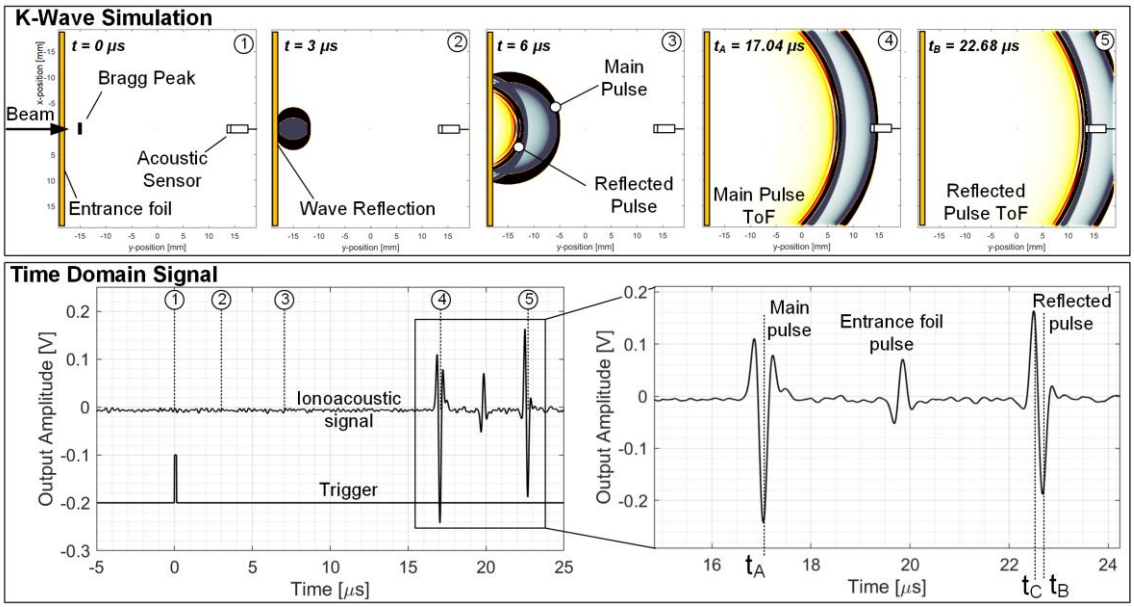

Figure 2.10– Comparison of dose distribution of protons with X-ray irradiation simulated in water

leads to a ProSD AFE Noise Figure as low as 0.6 dB. After electrical validation, the whole detector (composed by Acoustic Sensor + AFE + FPGA DSP) has been mounted on the water phantom energy absorber (Figure 2.1) and hit by a 20 MeV 120 ns pulsed proton beam at Maier-Leibniz Laboratory. Figure 2.1 shows the physical setup in which ProSD has been tested and validated. The water phantom has 40x30x50 cm^3 (H, W, L) volume filled by distilled water.The water temperature is measured with a thermocouple with 0.1 °C precision to correctly estimate the sound speed in water. The AS is immersed in the energy absorber and connected by a SMA coaxial cable to the LNA2. More in detail, the experimental setup photo in Figure 2.1 shows the AS and the beam entrance foil. Vacuum-air and air-water interfaces are made by a set of 11 µm-thick Titanium foil and 50 µm-thick Kapton foil, respectively. The acoustic wave propagates spherically in all directions. The most relevant signal (Main Pulse) propagates from the BP source volume towards the right side and reaches the acoustic sensor after 17.04 µs. The left part of the spherical pressure wave hits the water phantom entrance wall and comes back towards the sensor where it is read out after 22.68 µs. Figure 2.10 shows both k-Wave simulations of the spherical acoustic wave propagation (cross section) and the measured acoustic pulses at the ProSD AFE+DSP output after 100 beam shots averaging (to increase SNR and signal quality vs. noise). An external trigger, encoding the beam shot start instant, comes from the accelerator control stages up to the acoustic DSP. Figure 2.10 highlights five distinct instants:

1) 0 µs, the beam starts, ideally instantaneously hits the water phantom energy absorber and a trigger is sent to ProSD;
2) 3 µs, the left side of the acoustic spherical wave hits the Kapton foil and is reflected;
3) 6 µs, the acoustic signal is travelling toward the AS;

4) 17.04 μs, the acoustic wave generated in the BP Volume hits the AS;
5) 22.68 μs, reflected acoustic waves is read out by the AS.

The acoustic signal track (bottom part in Figure 2.10) is composed by three successive time pulses:

- Main Pulse is the signal coming from BP_{VOLUME} and propagating directly to the sensor;
- Entrance Foil Pulse is the acoustic pulse due to the beam transition from air to the water phantom through the entrance foil (not shown in k-Wave simulations);
- Reflected Pulse is the pulse generated by the BP volume sound source which propagates spherically, collides with the beam entrance foil (in the direction opposite to that of the entrance foil) and is read-out by the AS (covering at the end a longer path and therefore being the last pulse detected by the sensor).

The analog track in Figure 2.10 is then converted into digital domain by the A-to-D converter and provided to the acoustic DSP that calculates the ToF as follows:

$$BP_{DEPTH} = \left(\frac{(t_B - t_A) \cdot c_w}{2}\right) - \left(\frac{t_B - t_C}{2} \cdot c_w\right) \qquad \textit{Eq. 2.9}$$

where:

- t_A is the arrival instant of the main pulse (negative peak), equal to 17.04 μs;
- t_B is the arrival instant of the negative peak of the reflected pulse (negative peak), equal to 22.68μs;
- t_C is the arrival instant of the positive peak of the reflected wave and is equal to 22.50 μs;

cw is the water sound speed at 22.3°C temperature, equal to 1492 m/s. Hence, t_B-t_A is the time distance between the main signal and the Kapton foil signal reflection, respectively. The tC-tB term is a correction term that considers the relative position between the sources of the acoustic signals and the Bragg Peak. This term has to be introduced because the acoustic wave is generated at the point of maximum gradient of the Bragg curve. Hence, the tC-tB term takes into account the different location between the pressure wave source and the BP. Now that the main characteristics of the signals that propagate within the ionoacoustic setup have been defined, the BP localization technique/performance will be presented in two different and significative scenarios:

- a single beam shot (Nshot=1) to measure the achievable precision with a total deposited dose so low as 0.8 Gy;
- after real-time averaging 100 beam shots (Nshot=100 and 80 Gy total deposited dose at the BP) using a clear and almost noise-free acoustic pulse.

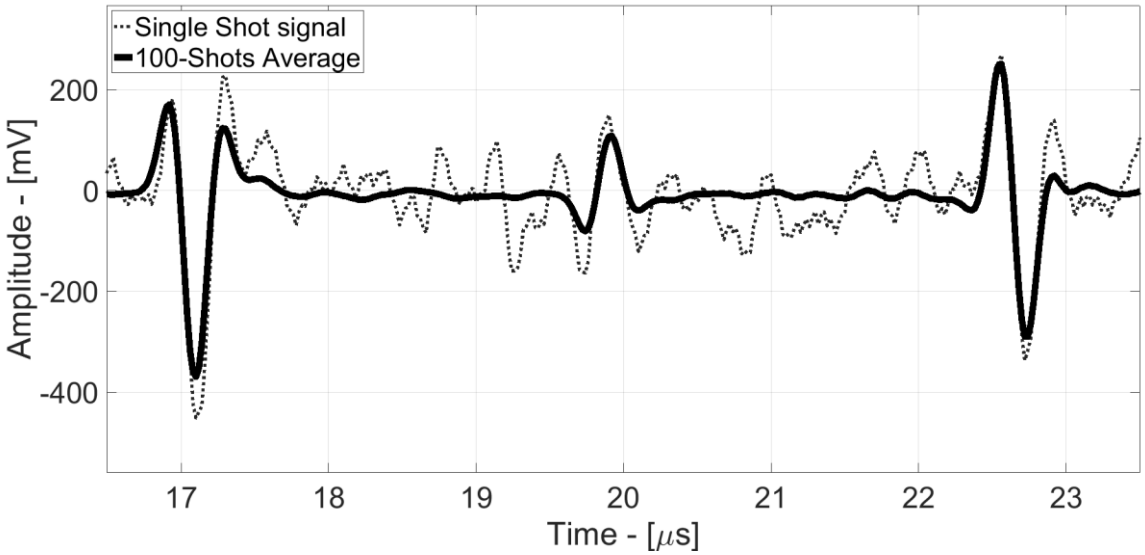

Figure 2.11– Comparison of dose distribution of protons with X-ray irradiation simulated in water

C. N_{shot}=1 Proton Sound Detection

A specific test has been performed using a single beam shot, thus delivering 0.8 Gy at the BP. Figure 2.11 reports the single-shot measured time-domain acoustic signal at the A-to-D converter output (and rescaling into analog dynamic range), generated by a 0.8 Gy BP dose deposition at 4060 μm distance from the entrance foil (according to Geant4 simulations) and 64 mVRMS noise power. This scenario is particularly relevant for possible clinical applications, since the main requirement is to obtain high precision with a dose compatible with clinical treatments (typically in the 100-101 Gy range) and more importantly without stressing the energy absorber by extra-doses depositions for beam calibration. In this scenario, the noise power is higher than 100 N_{SHOTS} scenario because averaging is not performed. However both the main and the reflected pulses are clearly distinguishable from background noise whereas entrance foil signal is quite hidden by noise (see Figure 2.11). In particular, the single beam shot measurement has been repeated for several iterations and the histogram has been produced representing the measured BP statistics (vs. 8000 iterations) in Figure 2.12. The resulting proton beam depth (i.e. BP volume position) is 4073 μm from entrance foil, to be compared with 4060 μm BP depth from Geant4 simulations. 13 μm accuracy is 0.34 % of the BP depth, thus proving the capability of this technique to provide accurate localization of the BP position even in case of single-shot 0.8 Gy dose scenario. The main sources of this deviation are small changes in water properties on sound propagation and non-negligible Geant4 simulation resolution errors.

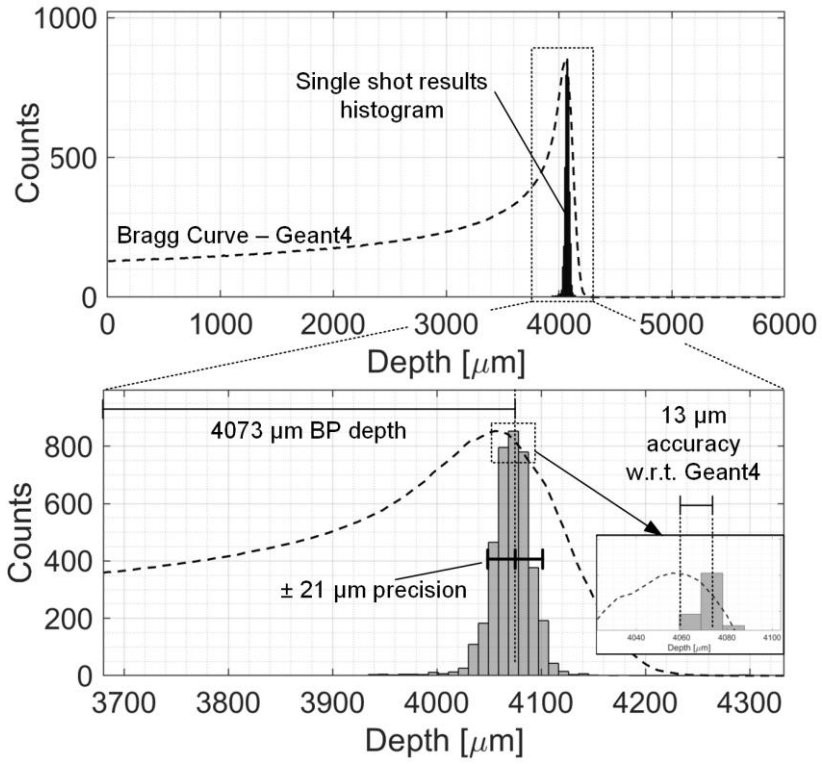

Figure 2.12– Comparison of dose distribution of protons with X-ray irradiation simulated in water

The observed precision (statistic distribution variance σ) of the BP localization is equal to 21 µm. 21 µm precision corresponds to just 0.5% of the proton beam range depth (i.e. BP volume position), equal to 4060 µm. Moreover, this measurement precision can be compared to the BP_{FWHM} which is 320 µm, resulting in 6.6 % relative error.

D. N_{Shot}=100 Proton Sound Detection

After evaluating the ProSD performance by processing a single shot signal, an high precision (at higher dose of 80 Gy) scenario is evaluated (bold line in Figure 2.11). The acoustic time track in Figure 2.11 has been achieved after 100 shots averaging (6.4 mV_{RMS} ProSD AFE output noise power), resulting in 32 dB SNR against 12 dB of single shot signal. Eq. 2.9 has been applied to 100 N_{SHOTS} averaging signal track. The variation of the measured BP depth caused by random noise variance (with 100 N_{SHOTS} real-time averaging) is equal to 3 µm (against 21 µm precision at single shot), to be compared with 4060 µm mean value, leading to a relative error as small as 0.07%. Finally, an intermediate scenario (more similar to clinical applications at max 8 Gy dose) with 10 available beam shots for averaging (and thus 10 dB SNR increase) allows to achieve a final SNR of 22 dB and a measurement precision of 7.5 µm, while delivering a relatively limited 8 Gy total dose. Table 2.4 summarizes the main results obtained in the presented experimental scenarios. Clearly, the SNR has a big impact on measurement precision, since higher noise fluctuations w.r.t. the signal amplitude can introduce higher measurement error on the BP position.

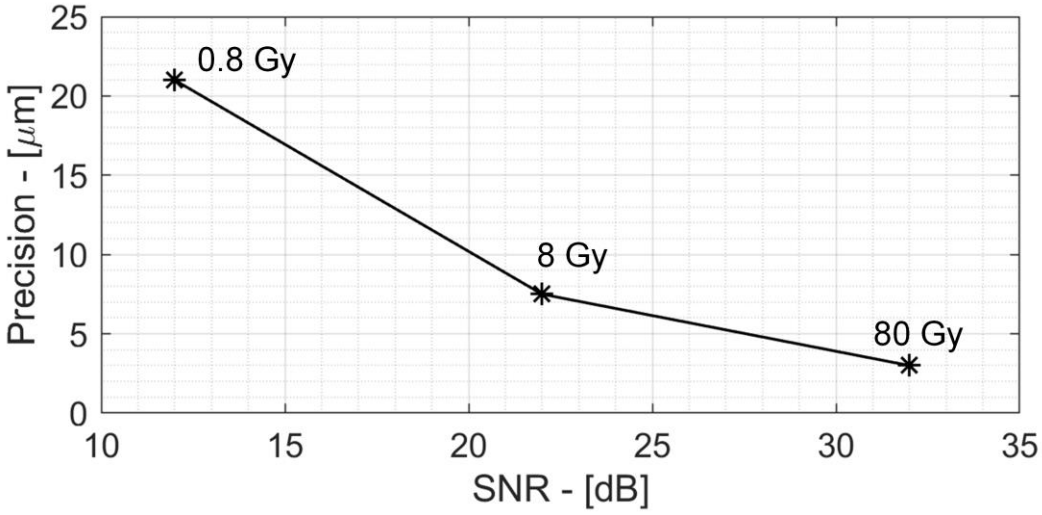

Figure 2.13– Comparison of dose distribution of protons with X-ray irradiation simulated in water

Table 2.4 – Acoustic AFE Analog Section Parameters

Parameter	**Single Shot**	**10-Shots**	**100-Shots**
SNR	12 dB	22 dB	32 dB
Dose	0.8 Gy	8 Gy	80 Gy
BP position	4073 µm	4073 µm	4073 µm
Precision	3 µm	7.5 µm	21 µm
Relative Error (%)	0.5 %	0.2 %	0.07%
Accuracy w.r.t. Geant4	13 µm	13 µm	13 µm

Figure 2.13 illustrates the impact of SNR on the measurement precision by comparing the results of the experimental scenarios listed in Table 2.4. It is possible to observe that for 12 dB SNR the precision is 21 µm, the precision steadily improves up to 7.5 µm for 24 dB SNR and 3 µm for 32 dB SNR. These results highlight the precision of the ionoacoustic technique that allow to localize the position of the BP with an uncertainty equal to 6.5%, 2.3% and 0.9% of the size of the BP_{FWHM} (320 µm) respectively for 12 dB, 22 dB and 32 dB SNR.

2.6. Comparison with State of the Art

The hereby presented ProSD achieves two main improvements w.r.t. previous experiments [4] with 20 MeV protons summarized in Table 2.5.

- Higher SNR thanks to the additional filtering stage specifically matched to the signal frequency, which improves the system performance by lowering the noise power by 6 dB in the analog domain, thus leading to an improved measurement precision;
- Real-time operation thanks to a dedicated HW DSP, that allows to online extrapolate the main experimental results while performing the experiment (i.e. information on the BP location is available shortly after the beam shot with latency below 100 µs). This is a key feature for envisioned medical applications since it potentially allows making corrections between each beam shot to compensate for mismatch between the target BP location (i.e. the treatment volume) and the actual BP location, caused for example by unwanted patient movements (breathing, hearth beating).

In order to highlight the advancements for future medical applications given by higher precision (and/or higher single shot SNR) sound detection, Eq. 2.10 shows the number of beam shots that needs to be averaged to have a certain increase in SNR.

$$\Delta SNR = 10log_{10}(N_{SHOTS}) \qquad Eq.\ 2.10$$

Considering the 6 dB increase in SNR w.r.t Assmann et al., ProSD achieves the same measurement precision with only 25% of the dose.

Table 2.5 – Acoustic AFE Analog Section Parameters

Parameter	**This work**	**Assman et al., 2015 [4]**
Proton Energy	20 MeV	20 MeV
Real-time operation	Yes	No
Main Features	LNA, LPF, HW DSP, SW DSP	LNA, SW DSP
SNR for 1 shot (0.8 Gy)	12 dB	6 dB
Accuracy w.r.t. Geant4 simulations	13 µm	87 µm
Single shot precision w.r.t. BP position	21 µm (0.5%)	45 µm
10 N_{SHOT} precision w.r.t. BP position	7.5 µm (0.18 %)	-
N_{SHOTS} to achieve 7.5 µm precision	10	40
Dose to achieve 7.5 µm precision	8 Gy	32 Gy

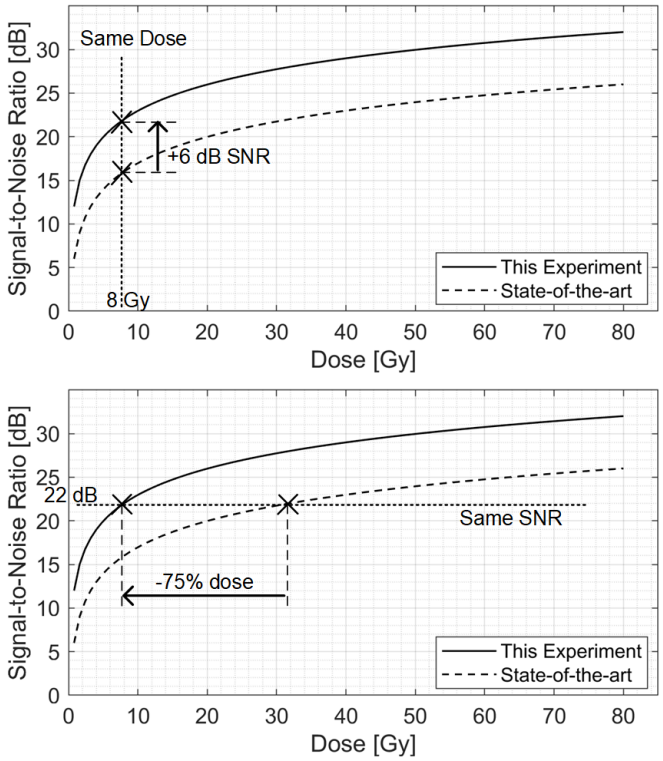

Figure 2.14– Comparison of dose distribution of protons with X-ray irradiation simulated in water

This result is clearly shown in Figure 2.14, where the vertical axis represents the final SNR after acquiring and averaging NSHOTS (0.8 Gy/shot), and the horizontal axis represents the total dose (NSHOTS times the single shot dose). Considering the 10-shots scenario corresponding to 8 Gy total dose, ProSD achieves 22 dB SNR whereas [4] achieves only 16 dB SNR (see in Figure 2.14, top). On the other hand, to achieve said 22 dB SNR, [4] needs to average four times the number of beam shots w.r.t. ProSD, thus requiring a total dose of 32 Gy (40 beam shots), to be compared with 8 Gy and 10 beam shots of ProSD. This result is particularly relevant for future clinical applications since it highlights the capability of dedicated detectors to precisely locate the dose deposition, possibly minimizing collateral dose to the patient.

2.7. Experimental Results Conclusions

In this Chapter the design and electrical/experimental validation of a Proton Sound Detector specifically dedicated to pre-clinical ionoacoustic experimental setups have been presented. The detector has been tested with a pre-clinical 20 MeV beam of protons and has obtained a precision in the localization of the Bragg peak of 21 μm with a 0.8 Gy dose, achieving double the state-of-the-art precision in same conditions. The results presented in this work show how the instrumentation used in ionacoustic experiments has ample room for improvement. In fact, the use of dedicated (although standard/not integrated) electronics allowed for a 75% dose reduction compared to previous works to achieve the same precision. The ionacoustic technique has the potential to establish itself

as a tool for the characterization and calibration of particle beams thanks to the simplicity of the required instrumentation and the high obtainable precision, but one of the limits for this technique to be appliable in clinical scenarios is the high dose (not compatible with medical treatments) necessary to obtain such high precision. Moreover, other issues for clinical applications regards the lower acoustic signal frequency w.r.t. pre-clinical scenarios (with corresponding lower resolution), the inhomogeneous medium and acoustic coupling mismatch between different tissues. It is therefore essential to improve the detector (intended as acoustic sensor, electronics and DSP) to achieve higher SNR for a given low dose. This improvement cannot rely on averaging multiple beam shots, as it is an inefficient technique that require a large dose increase to achieve a moderate improvement in precision. Instead, it is necessary to adopt dedicated acoustic sensors that allow obtaining high precisions for a single low dose shot. This can be achieved for example by using multichannel sensors that acquire multiple waveforms for the same beam shot, therefore further increasing the SNR and precision for the same dose. However multichannel sensors cannot rely on standard electronics but require dedicated integrated electronics and hardware-based DSP to fully exploit their potentials, obtaining high precision Bragg peak localization in space in real-time with limited detector harness and at low doses. Hence, a strong design effort on all detector parts is required to bring the ionoacoustic technique to clinical applications.

3.

Modelling the Ionoacoustic Effect as a Linear Time-Invariant System

Chapter Abstract - This chapter presents the modelling of the ionoacoustic phenomenon as a Linear Time-Invariant system (called iono-LTI). The model proposed here allows to obtain in a simple and rapid way a representation of the ionoacoustic signal as a function of the characteristics of the particle beam that generates it. This model is much more practical and easier to use than classic simulations that use different software tools and require long simulation times. The hereby presented iono-LTI model will be validated by comparing its time and frequency domain results with real ionoacoustic signals recorded during beam experiments. Finally, it will be used to show the criticalities of clinical energy scenarios compared to sub-clinical ones, underlining the need for a dedicated detector in clinical applications.

3.1 Ionoacoustic Signal Dependence on Pulse Time and Stress Confinement

In the previous chapter the design of a dedicated Proton Sound Detector was presented. Experimental results have shown that by improving the detection electronics, a significant performance improvement over previous works can be achieved. During the same beam test we also investigated the ioacoustic effect in non-ideal beam conditions, and in particular when the pulse time no longer respects the stress confinement condition. A variable pulse time between 70 ns and 320 ns was used (compared to a stress confinement time of 220 ns), keeping the beam current (and therefore the dose deposition rate Gy/sec) constant. In particular, the dose is deposited in the Bragg peak at a rate of 6.6 Gy/μs (called dose deposition rate, dr(t)), as shown in Figure 3.1, where the stress confinement time (vertical dashed line) and the dose deposition rates are highlighted. The rising and falling edges last a few nanoseconds and the deposition is comparable to an ideal square wave. Figure 3.2 shows the ProSD output signal for different t_{pulse} values. It can be observed that both the amplitude and shape of the signal vary as a function of the pulse time. In particular, by increasing the pulse time (and therefore the deposited dose), the amplitude of the signal increases until the pulse time exceeds the stress confinement time.

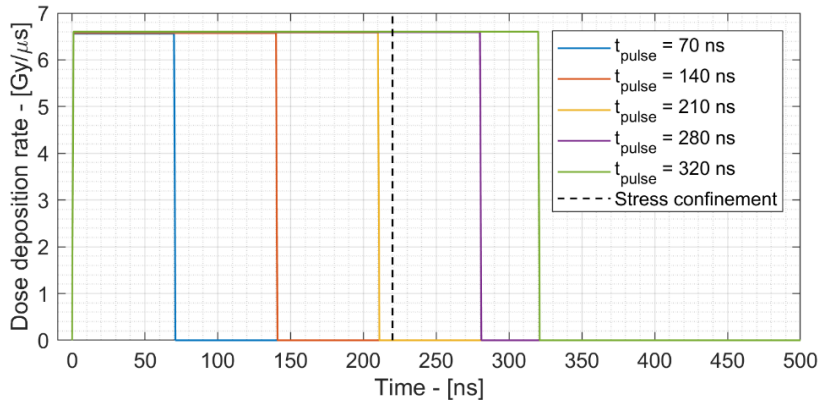

Figure 3.1 – Dose deposition rates dr(t) for different beam pulse lengths

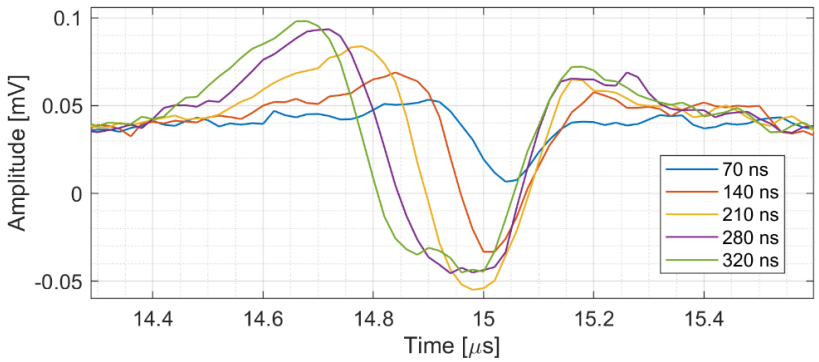

Figure 3.2 – Measured ionoacoustic signals for different beam pulse lengths

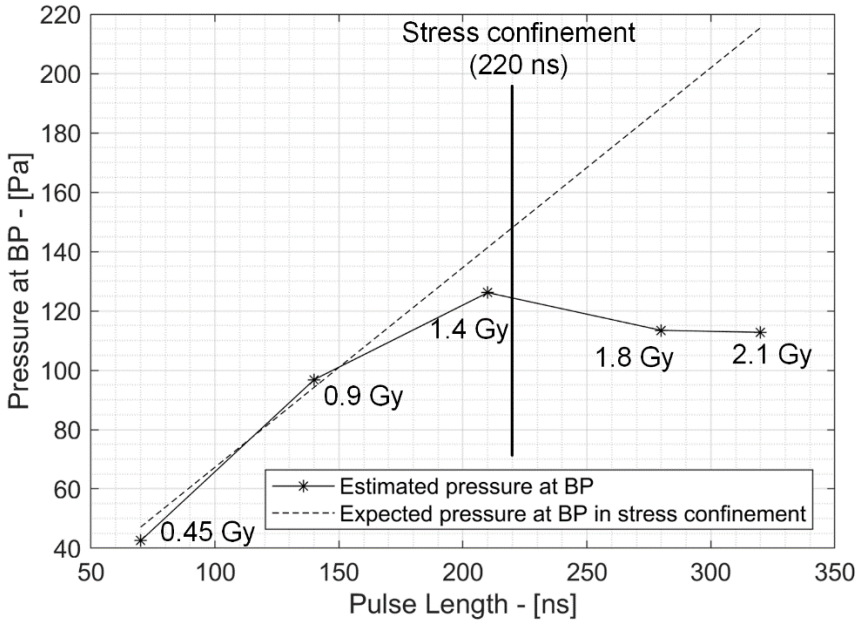

Figure 3.3 – Pressure amplitude at the Bragg peak for different pulse length with correspondent dose deposition, compared to the expected pressure increase for the same dose in stress confinement condition

Table 3.1 – Summary of acoustic signals characteristics for different beam pulses

Pulse Time	**Total dose at BP**	**Estimated Signal Amplitude at BP**	**Expected Signal Amplitude at BP (in stress confinement)**	**Dose at BP within stress confinement**	**Expected Signal Amplitude at BP (in stress confinement)**	**Ionoacoustic Efficiency (Output Pa vs input Gy)**
70 ns	0.45 Gy	42 Pa	46 Pa	0.45 Gy	46 Pa	93 Pa/Gy
140 ns	0.9 Gy	97 Pa	92 Pa	0.9 Gy	92 Pa	107 Pa/Gy
210 ns	1.4 Gy	126 Pa	143 Pa	1.4 Gy	143 Pa	90 Pa/Gy
280 ns	1.8 Gy	113 Pa	183 Pa	1.45 Gy	148 Pa	63 Pa/Gy
320 ns	2.1 Gy	112 Pa	214 Pa	1.45 Gy	148 Pa	53 Pa/Gy

This trend is shown in Figure 3.3, where the pressure at the Bragg peak is shown as the pulse time and the deposited dose vary. The dashed line shows the expected trend from the Eq. 2.5, shown below for convenience.

$$\Delta P_{BP} \cong \frac{\beta}{k \cdot C_V} \mathrm{D} = 102\ \mathrm{D} \qquad \textit{Eq. 2.5}$$

As it can be seen, the expected pressure value is close to the measured value under stress confinement conditions, whereas for longer pulse times an increase in dose does not correspond to an increase in peak pressure. Table 3.1 summarizes these scenarios and shows that a more accurate estimate of the peak pressure can be obtained by considering in Eq. 2.5 only the dose deposited before the stress confinement, while the dose deposited after stress confinement does not contribute to increase the pressure.

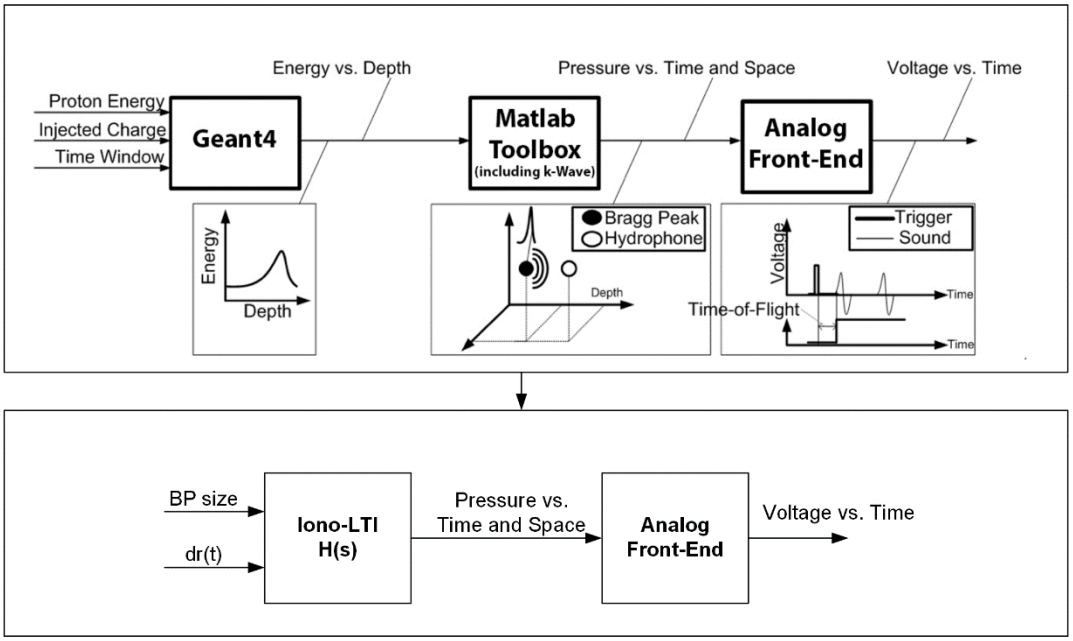

Figure 3.4 – Standard cross-domain model and proposed Iono-LTI system model

This phenomenon is particularly interesting in clinical scenarios, since the dose deposition time-shape influences the amplitude of the signal for a given dose and hence the SNR and the achievable precision. The last column of Table 3.1 shows the relationship between the amplitude of the output signal and the deposited dose, which can be defined as the efficiency of the ionoacoustic process. This value can be obtained from Eq. 2.5, and should be equal to b/(kCv) or 102 Pa/Gy. When the stress confinement is satisfied the measured values are close to the expected one, while when the pulse time increases this value progressively decreases, since the amplitude of the acoustic signal remains the same when the total deposited dose increases.

Taking a cue from these observations, we decided to deepen the modeling of the ionoacoustic phenomenon with two main objectives:

- To evaluate what are the characteristics of the ionoacoustic signal in different scenarios and different energies
- To obtain a tool that allows us to improve and facilitate the design of Proton Sound Detectors, starting from well-defined experimental conditions

The classical approach to obtain this model is shown in Figure 3.4, taken from [19] where a cross-domain model of the whole system is described. First, the beam is modeled using Geant4 to obtain a spatial dose distribution in one or more dimensions. Then, this dose distribution is converted into a pressure increase and used as an input for k-Wave, a Matlab toolbox that allows to simulate the propagation of acoustic waves. Finally, the signal acquired by ideal k-Wave virtual sensors is processed through a dedicated Matlab script that models the acoustic sensor and electronics frequency response and noise to finally obtain a realistic signal.

Such model is very complete and reliably describes the ionoacoustic phenomenon and detector. However, it is not user-friendly, requiring to use three different computational tools. Furthermore, k-Wave in particular is quite demanding in terms of simulation times and hardware required, and often the size of the simulated volume is severely limited by the amount of RAM of the PC used and by the simulation time, and therefore requires to use cloud-based services and/or the use of dedicated GPUs. Finally, such a model is not very suitable sweep-variable simulations, since they require various different simulations that can each last tens of hours. For this reason, we looked for a simpler model to quickly and accurately characterize different scenarios. We exploited the fact that the ionoacoustic phenomenon has the characteristics of linearity and time invariance and is therefore modelable as a linear time-invariant (LTI) system. Starting from the general characteristics of the Bragg curve (beam diameter and BP_{FWHM}) and from the deposition time profile of the dose deposition dr(t), this model allows to obtain the time domain waveform at the sensor. In the next section we will show how to derive the transfer function of the ionoacoustic LTI (Iono-LTI) system and show the ionoacoustic signals in different scenarios both in the time and frequency domain. Finally we will validate the results obtained from this model by comparing them with Figure 3.2 and with experimental data present in literature.

3.2 Ionoacoustic Linear Time-Independent System Modelling

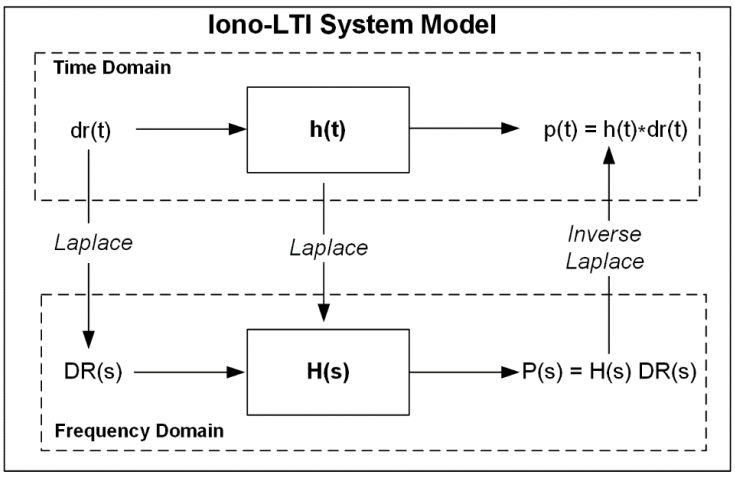

Figure 3.5 – Iono-LTI system Model scheme

Figure 3.5 shows how to model the ionacoustic effect as an LTI system. When the absorber is stimulated by an energy deposition much shorter than the stress confinement, the resulting pressure signal p(t) is equivalent to the impulse response of the system. Therefore, with reference to the Figure 3.5, when dr(t) is equal to δ(t), we can obtain the transfer function H(s) of the system by making the Laplace transform of the impulse response p(t). Finally, knowing H(s), it is possible to calculate p(t) for any value of dr(t).

A windowed sinusoid over a single period was used as the impulse response p(t). To estimate the signal frequency we have considered the fact that the BP_{FWHM} is equal to half the wavelength of the acoustic signal, and therefore the frequency can be estimated as $c_w/(2\ BP_{FWHM})$. Figure 3.6 shows the impulse response of the system, which is described by Eq. 3.1.

$$p_\delta\,(t) = \frac{\beta}{\mathrm{k}c_\mathrm{v}}\,\mathrm{D}\,\sin(\omega_0 t)\,rect(t) \qquad \textit{Eq. 3.1}$$

$$rect(t) = \begin{cases} 1 & if \quad 0 \leqslant t \leqslant \dfrac{2\pi}{\omega_0} \\ 0 & if \quad t > \dfrac{2\pi}{\omega_0} \end{cases}$$

The transfer function H(s) of the system is obtained by calculating the Laplace transform of the impulse response (Eq. 3.2).

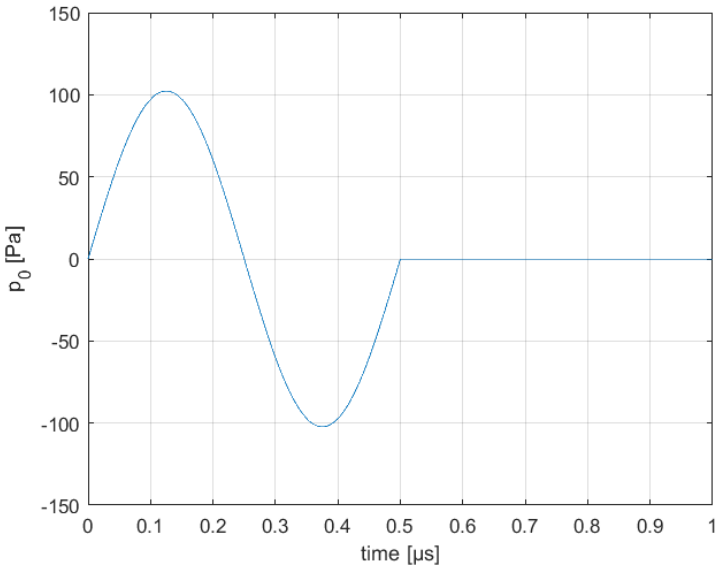

Figure 3.6 – Iono-LTI System impulse response in time domain

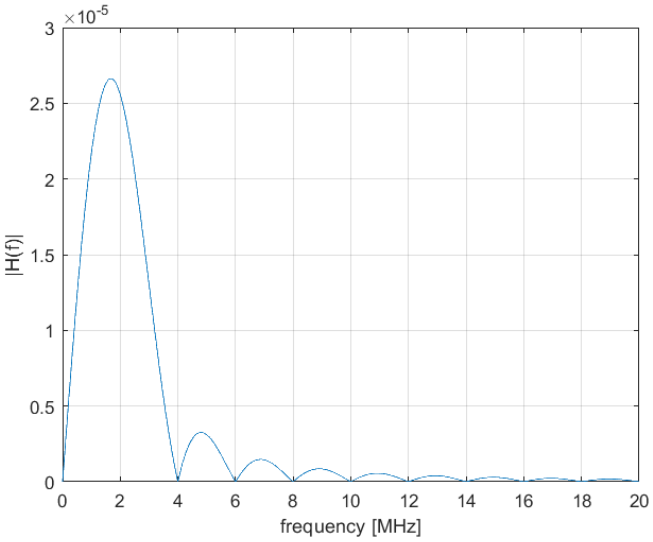

Figure 3.7 – Iono-LTI System frequency response

$$\mathcal{L}\{p\}(s) = H(s) = \frac{\beta}{kc_v} D \frac{\omega_0 \left(1 - e^{-\frac{2\pi s}{\omega_0}}\right)}{{\omega_0}^2 + s^2}$$

Eq. 3.2

$$H(f) = \frac{\beta}{kc_v} D \frac{\omega_0 \left(1 - e^{-\frac{4\pi^2 if}{\omega_0}}\right)}{{\omega_0}^2 + (2\pi i f)^2}$$

The frequency response of the system is plotted in Figure 3.7 and it feature a peak at 2 MHz (signal frequency) and its even harmonics.

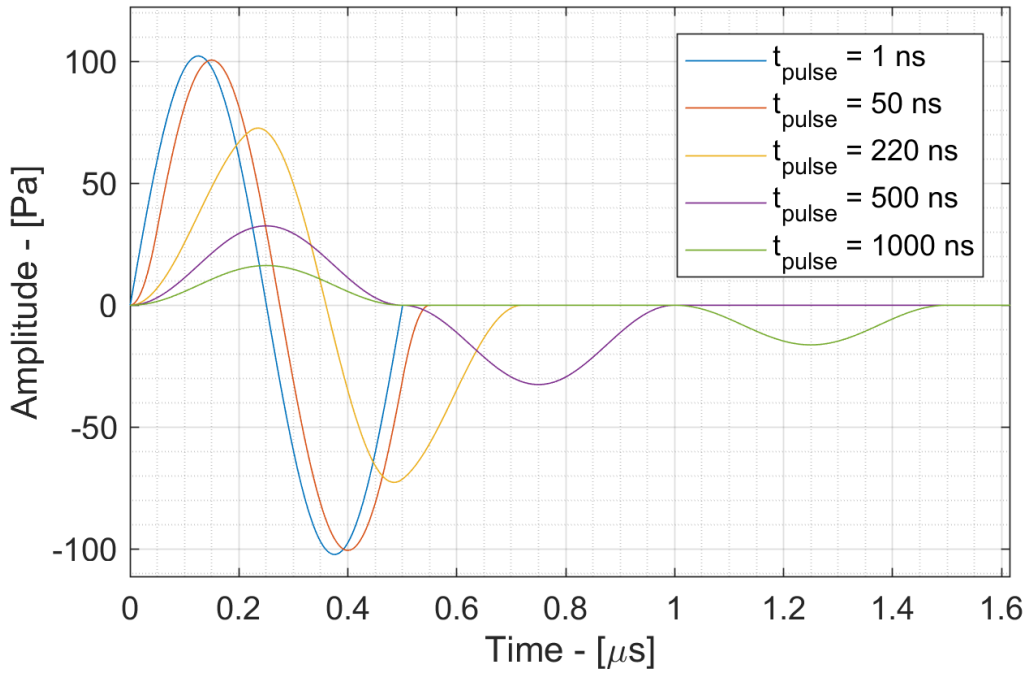

Figure 3.8 – Iono-LTI output signals for different input pulse lengths

The transfer function H(s) can be used to calculate the output pressure signal of the system when different input beam pulse shapes are used. Rectangular pulses are particularly interesting since the experimental results in Chapter 2 are achieved with such beam pulse shape. Thus, if DR(s) is the Laplace transform of a rectangular with t_{pulse} length and dr_0 dose deposition rate (Gy/sec), the output signal in Laplace domain is described by Eq. 3.3.

$$P(s) = H(s)DR(s) = dr_0\,\omega_0 \frac{\left(1 - e^{-\frac{2\pi}{\omega_0}s}\right)(1 - e^{-Ts})}{s({\omega_0}^2 + s^2)} \qquad \textit{Eq. 3.3}$$

$$P(f) = dr_0\omega_0 \frac{\left(1 - e^{-\frac{4\pi^2}{\omega_0}if}\right)\left(1 - e^{-2T\pi if}\right)}{2\pi if[{\omega_0}^2 - 4(\pi f)^2]}$$

Computing the inverse Laplace transform, we finally obtain the time domain ionoacoustic signal in response to a rectangular beam pulse.

The time domain signal p(t) is described in Eq. 3.4 and plotted in Figure 3.8 for different beam pulses and the same total dose deposition of 1 Gy. As expected, the 1 ns t_{pulse} is practically identical to the system impulse response. Its peak pressure is 102 Pa as expected from Eq. 2.5. The 50 ns pulse is again similar to the ideal impulse response of the system in terms of signal shape and amplitude. However, when the pulse time increases up to the 220 ns stress confinement time, the signal amplitude decreases and its duration increases. When the pulse time is higher than the stress confinement time, the

positive and negative parts of the signal are separated. Each part now represents the step response of the system and happens at the rising edge and falling edge of the rectangular pulse. Moreover, it is interesting to note that the dose deposition is the same in all cases, but the signal amplitude decreases with the beam pulse length, suggesting that only the dose deposited within the stress confinement concur in increasing the pressure amplitude. This effect is consistent with the stress confinement condition which is related to the isochoric behavior of the system. If the condition is met, energy deposition occurs faster than volume expansion, and the process is isochoric. If, on the other hand, the deposition of energy is slower, the system will begin to react by expanding (and propagating as an acoustic wave), therefore a further deposition of energy will not correspond to an increase in pressure.

$$p(t) = dr_0 \frac{1}{\omega_0} \begin{cases} 1 - cos(\omega_0 t) & if \quad t < T \\ cos[\omega_0(t-T)] - cos(\omega_0 t) & if \quad T < t < \frac{2\pi}{\omega_0} \\ cos[\omega_0(t-T)] - 1 & if \quad \frac{2\pi}{\omega_0} < t < \frac{2\pi}{\omega_0} + T \\ 0 & if \quad t > \frac{2\pi}{\omega_0} + T \end{cases}$$

if $T < \frac{2\pi}{\omega_0}$ and *Eq. 3.4*

$$p(t) = dr_0 \frac{1}{\omega_0} \begin{cases} 1 - cos(\omega_0 t) & if \quad t < \frac{2\pi}{\omega_0} \\ 0 & if \quad \frac{2\pi}{\omega_0} < t < T \\ cos[\omega_0(t-T)] - 1 & if \quad T < t < \frac{2\pi}{\omega_0} + T \\ 0 & if \quad t > \frac{2\pi}{\omega_0} + T \end{cases}$$

if $T > \frac{2\pi}{\omega_0}$

3.3 Iono-LTI System Validation Against Experimental Results

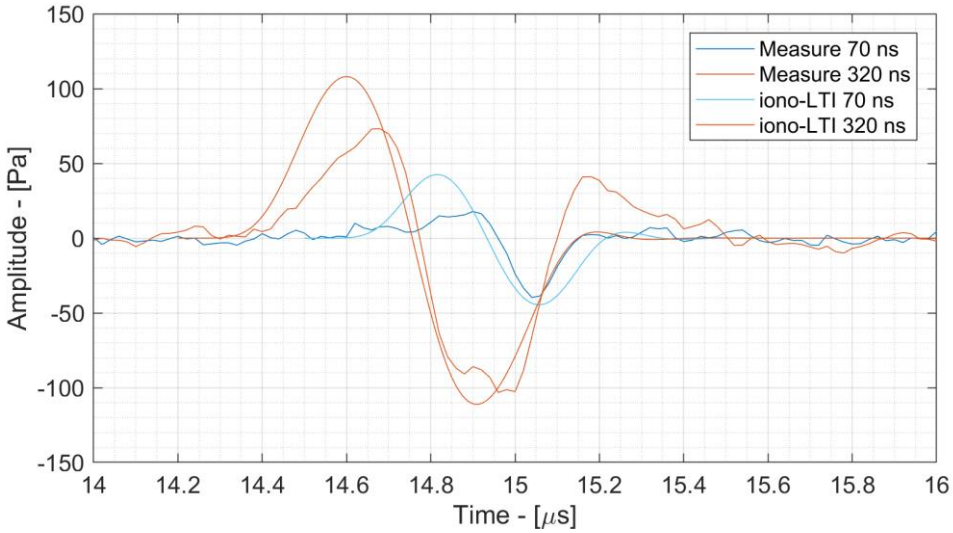

Figure 3.9 – Comparison between Iono-LTI signals and measured signals with 70 ns and 320 ns beam pulse lengths

To validate the results of the model, a comparison was made between the measurements with 70 ns and 320 ns pulse time reported in Figure 3.2 and the same scenarios obtained with the model. However, the simulated signals reported in the previous section refer to the signal at the BP, while the measured ones are acquired by a sensor and have been processed by the frequency response of the ProSD described in Chapter 2.

To make a meaningful comparison, the signals produced by the Iono-LTI were also processed by the same analog chain reported in Chapter 2, and the measured pressures were rescaled by a factor of 16 to compensate for the attenuation due to the distance between the sensor. and the BP. Figure 3.9 shows the result of this comparison in time domain, where the signal shape and amplitude are well represented.

3.4 Iono-LTI Applied to Clinical Scenarios

The ProSD project aims to develop advanced detectors for ionacoustic experiments. Once the 20 MeV scenario has been characterized, it is therefore necessary to move to higher energies to highlight what are the difficulties in achieving sub-mm precision with clinical beams. These scenarios are typically characterized by lower dose depositions than sub-clinical experiments, as was shown in Chapter 1.2. The first step in designing a detector optimized for clinical energies is therefore to characterize the signal in terms of amplitude and frequency. In particular, this section will show the characteristics of two proton beams scenarios at 65 MeV and 200 MeV, which represent respectively the minimum and maximum limit of clinical energies. The main characteristics of these two scenarios are listed in Table 3.2. Compared with the case at 20 MeV, it is immediately clear that the deposited dose is much lower, of the order of 50 mGy/shot at 65 MeV and 10 mGy/shot at 200 MeV. Compared to the 800 mGy/shot of the experiment described in Chapter 2, the reduction is of 1/16 and 1/80 respectively. The pressure generated at the Bragg Peak is proportional to the deposited dose and therefore undergoes the same reduction. This fact immediately shows the criticality of these scenarios in terms of SNR and explains why state of the art average 100-1000 beam shots to observe an acoustic signal. Finally, clinical accelerators have not been designed to optimize the ioacoustic signal, and therefore have rather long pulse times that often do operate in stress confinement condition.

To characterize these scenarios, the Iono-LTI was then applied to two different pulse lengths scenarios. The first, equal to half the stress confinement, represents an optimal but realistic situation (called fast beam), while the second, in which the pulse time is twice the stress confinement, represents a more critical situation but likely to be found in hadron therapy centers (called slow beam). In both cases, the deposited dose per shot is constant and equal to 50 mGy/shot and 10 mGy/shot (65 MeV and 200 MeV). The same 24 dB attenuation has been applied to estimate the pressure at the sensor surface.

Table 3.2 – Pre-Clinical and clinical scenarios comparison

Proton Energy	Protons per shot	Beam range in water	BP_{FWHM}	Stress Confinement	Dose/shot at BP	Pressure at BP
20 MeV	10^6	4.1 mm	0.3 mm	220 ns	800 mGy	80 Pa
65 MeV	10^6	38 mm	2.9 mm	1.96 µs	50 mGy	5 Pa
200 MeV	10^6	247 mm	19.2 mm	12.9 µs	10 mGy	1 Pa

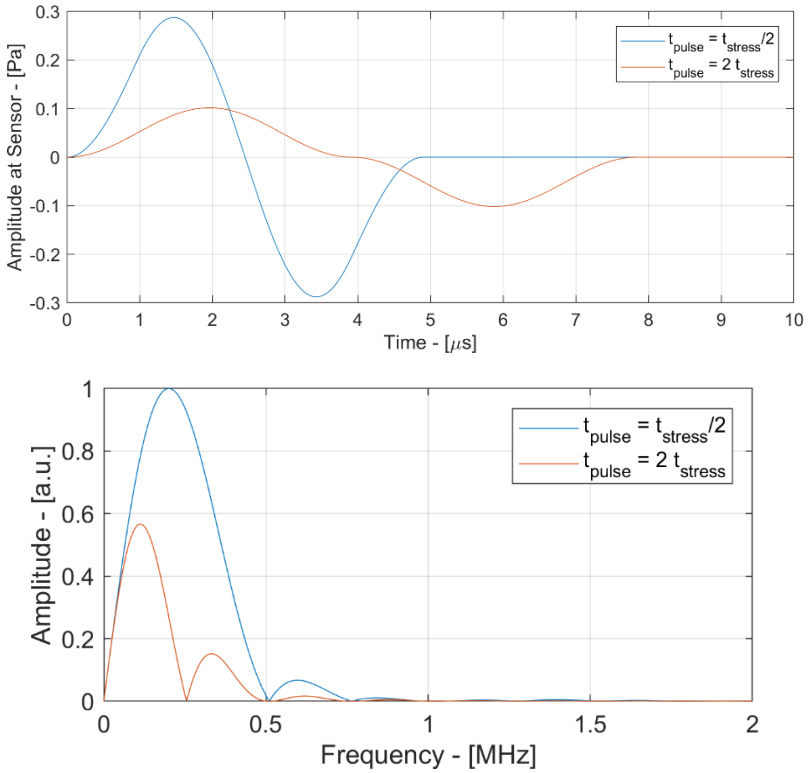

Figure 3.10 – 65 MeV protons time and frequency domain signals in "fast beam" scenario (pulse time equal to half the stress confinement time) and "slow beam" scenario (pulse time equal to double the stress confinement time)

Figure 3.10 shows the time domain ionoacoustic signal generated by the 65 MeV protons beam. In the fast beam case, the pressure at the sensor surface is 290 mPa, whereas if stress confinement is not fulfilled the signal amplitude is reduced to one-third, 100 mPa. The signal spectrum is shown in Figure 3.10 - bottom. The main frequency components are at 200 kHz and 100 kHz depending on beam pulse length. Most commercial hydrophones used by literature for high-energy experiments have 200 kHz bandwidth and ~30 mPa_{RMS} noise power. The single-shot SNR at the sensor output is 16 dB for the fast beam case and 7 dB for the slow beam case. These SNR values are referred at the output of the sensor, whereas the conditioning electronics front-end may significantly lower the SNR by 3-6 dB, especially if it is not dedicated and made by off-the-shelf components. Whereas 16 dB SNR are sufficient to localize the BP, with 7 dB SNR the ionoacoustic signal spike is almost buried in random noise fluctuation. Thus, such slow beam scenario would require averaging to improve the SNR and localize the BP. In particular, to compensate the 9 dB SNR difference between the fast and slow beam scenarios, 8 beam shots need to be averaged, for a total dose deposition of 400 mGy.

The 65 MeV scenario is therefore potentially critical even in the optimal scenario (fast beam), and any factor that contributes to worsening the SNR (poor electronics performance, greater detector distance, environmental noise and interferers) forces to use averaging with the consequent dose increase.

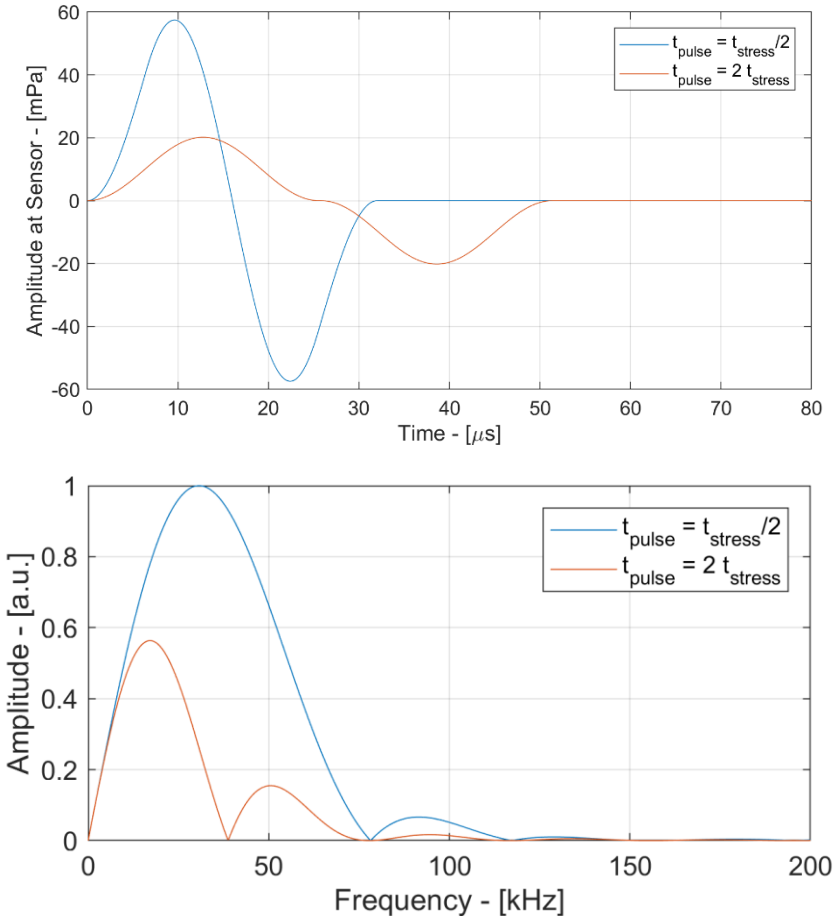

Figure 3.11 – 200 MeV protons time and frequency domain signals in "fast beam" scenario (pulse time equal to half the stress confinement time) and "slow beam" scenario (pulse time equal to double the stress confinement time)

The 200 MeV scenario is even more critical, as can be seen from the signal time domain amplitude shown in Figure 3.11. In the fast beam scenario, the pressure at the sensor is equal to 60 mPa and drops to 20 mPa in the slow beam scenario, while the peak frequency is 40 kHz and 20 kHz, respectively (Figure 3.11). These low amplitudes mean that even in optimal conditions the SNR to the sensor is only 3 dB (again, without considering the electronics noise), while in the slow beam scenario the SNR is negative and equal to -6.5 dB. This means that 8 beam shots and 70 beam shots are needed respectively to reach a sufficient SNR for a localization (about 12 dB). This quick estimate was made considering an ideal condition, i.e. neglecting any noise source other than the sensor. In fact, in literature it can be seen that even 1000 shots of the beam are averaged to obtain a clear signal. However, averaging is not efficient in terms of total dose deposition. Therefore, to successfully operate in critical scenarios, the SNR increase must be obtained in the analog domain and not in post-processing. It is therefore necessary to improve the sensor and the electronics to acquire weak signals while using limited total doses. The next chapter will take up the strategy started in Chapter 2 and show how to achieve a significant improvement in SNR at the detector level.

4.

High-Resolution Proton Sound Detector Design

Chapter Abstract - This chapter outlines the design of a dedicated detector consisting of a multichannel sensor, an application-specific integrated circuit (ASIC) and real-time digital signal processing. It will be shown how in the clinical setting the classical time domain average approach is not applicable and therefore how the increase of the signal to noise ratio must be done at the detector level. A time domain averaging strategy will be proposed which however requires aggressive miniaturization of the electronics, which must then be implemented on an ASIC. The design and characterization of a dedicated ASIC that processes the signals coming from a multichannel sensor and converts them into digital will then be shown, where a hardware-implemented algorithm allows a low-noise localization of the Bragg peak. The ASIC, the multi-channel sensor and the digital stages make up the so-called High-Resolution Proton Sound Detector, which promises to improve the signal-to-noise ratio at the same dose by 18 dB compared to single-channel detectors. This improvement in SNR allows to decrease by a factor of 64 the dose required to achieve a certain precision. This result is very promising in view of a future clinical application of the ionoacoustic technique.

4.1 Improving the Signal-to-Noise Ratio in Analog Domain

Clinical scenarios are characterized by low dose and very weak signals resulting in a low or negative SNR which in the literature is increased by making massive use of post-processing and signal averaging in digital domain. This approach is fine for characterizing the physical phenomenon, but it is limiting for possible clinical applications of the technique, as it involves a significant increase in the deposited dose. In order to acquire weak signals at clinical doses it is therefore necessary to continue with the approach begun in Chapter 2 and therefore to aim at improving the SNR in the analog domain at the detector level. The next section will discuss the most important limitation of averaging when applied in clinical scenarios, and a different approach to improve the SNR at the sensor level will then be presented.

A. Temporal Averaging Limitations in Clinical Scenarios

Temporal averaging, performed by acquiring different time realization of the same signal, increases the SNR following Eq. 4.1, where SNR_{Nsh} is the SNR achieved after averaging N_{sh} shots with a single shot SNR equal to SNR_{1sh}.

$$SNR_{Nsh} = SNR_{1Sh} + 10\log_{10} N_{Sh} \qquad \textit{Eq. 4.1}$$

However, averaging has two significand drawbacks, especially relevant when applied to clinical scenarios and beam characterization in general.

First, in clinical scenarios the SNR increase after N_{sh} comes at the cost of an additional dose. Literature requires 100-1000 averages to perform measurements in clinical scenarios, meaning that a 20-30 dB SNR increase is needed to achieve a clear ionoacoustic signal and to localize the BP with the reported precision, as can be seen in Figure 4.1 *(left)*. However, this results in an additional dose deposition, as shown in Figure 4.1 *(right)* for a typical clinical scenarios with 10 mGy dose/shot. A 20 dB SNR increase would require a total of 1 Gy additional dose, whereas to increase the SNR by 30 dB SNR the additional dose would rise up to 10 Gy.

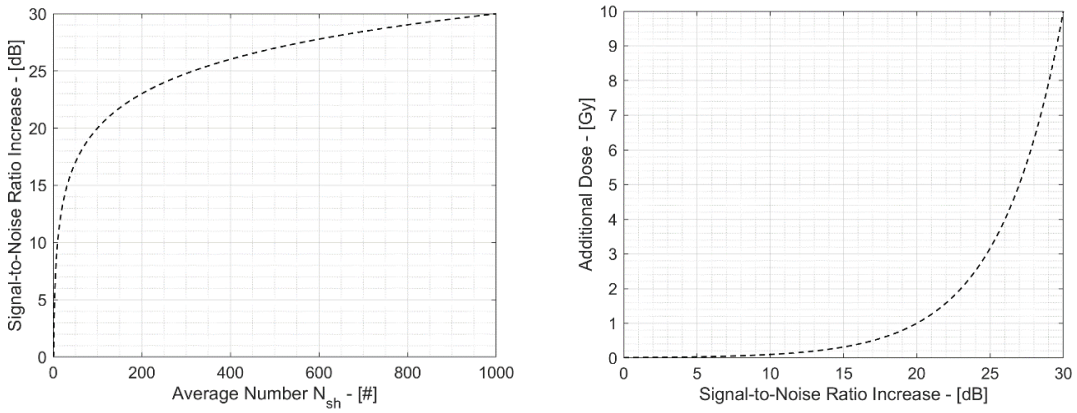

Figure 4.1 – *SNR increase with averaging (left) and resulting increase in dose deposition (right)*

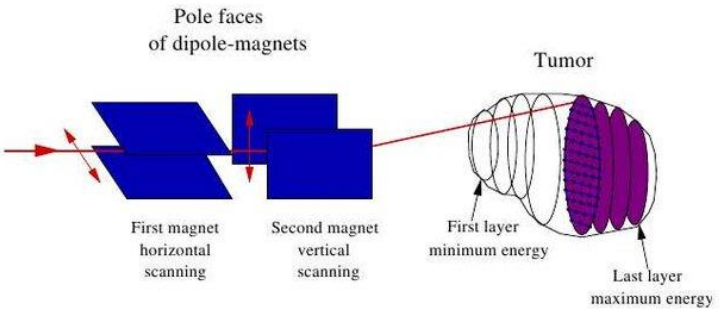

Figure 4.2 – *Active Beam Scanning allows to selectively deliver the dose to different area of the treatment volume [8]*

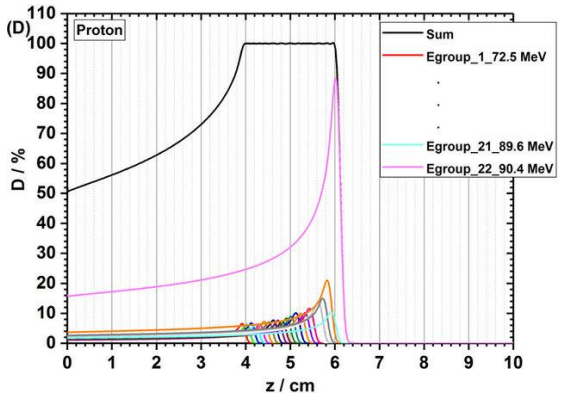

Figure 4.3 – *Multiple pristine Bragg curves and cumulative Bragg cure with Spread-Out Bragg Peak [9]*

By drastically increasing the total dose, the temporal averaging approach goes in the opposite direction of what is needed in clinical scenarios, that is achieving a high precision localization with low doses.

The second drawback of the time average is that it requires that the physical phenomenon is perfectly reproduced at each beam shot. In reality, many parameters of particle beams experiences various degree of instability, such as beam oscillations along the horizontal and vertical axes or fluctuations in the beam current that occur at different time scales and can be seen in different shots. In these conditions, averaging doesn't allow to characterize those fluctuation and may give a false representation of the beam characteristics, in the same way a long exposure photography of a moving object results in a blurred image.

This drawback is particularly relevant in modern hadron therapy treatments that uses advanced beam steering techniques to perform 2D/3D raster scans of the treatment volume. Modern hadron therapy treatments utilize a small-diameter (5-10 mm) pencil-like beam that is constantly modulated in energy and position to perform a scan of the treatment volume and increase the dose deposition conformity. This feature is shown in Figure 4.2 where the treatment volume (tumor location) is divided in various layers. Each layer is then treated by changing the beam energy (and thus its penetration depth) to match the layer depth.

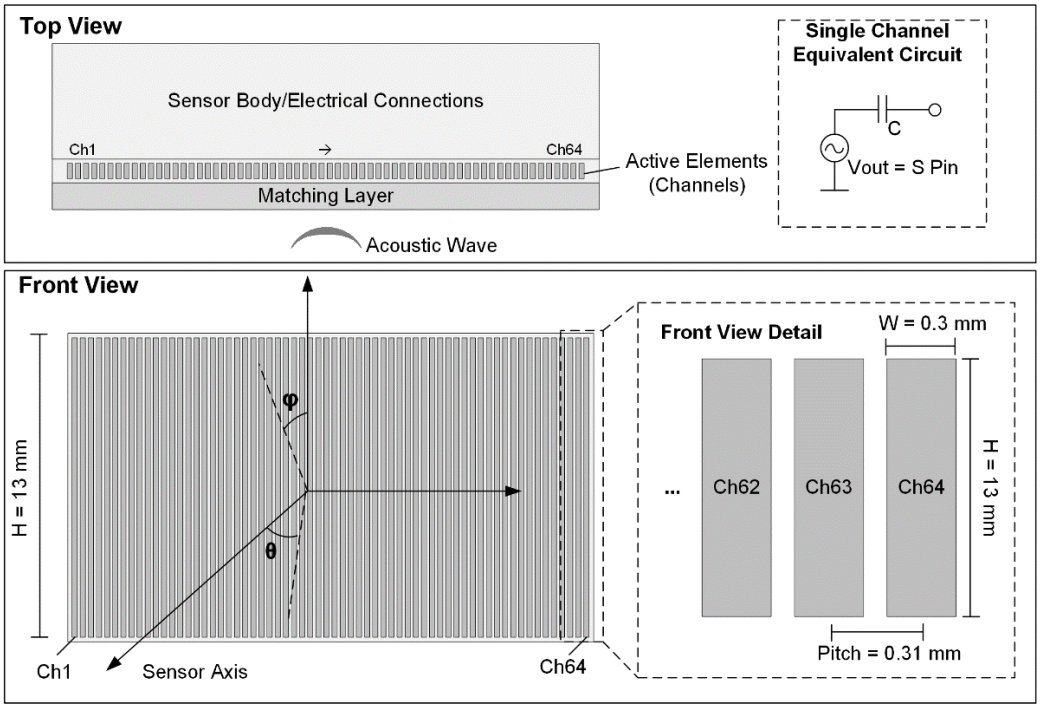

Figure 4.4– Multichannel sensor structure and single channel equivalent electrical scheme

The pencil-like beam is scanned by means of a two sets of bending magnets to deliver the desired dose to all the layer surface, performing a raster scan. Then, the beam energy is changed to deposit the dose to a different layer, and this 3D scan is performed to the whole tumor volume. However, when a layer is selected, the Bragg curve shape implies that a certain dose is deposited also in the less deep layers. To compensate this feature, Figure 4.3 shows that each layer is irradiated with a different dose so that when the dose depositions of all layers is added, a homogeneous dose deposition in the treatment volume is achieved. Such cumulative Bragg curve is called Spread-Out Bragg Peak (SOBP) and is shown in black in Figure 4.3. When considering the ionoacoustic effect, such beam active scanning means that the acoustic source location constantly changes position, thus leading to different acoustic signal time of arrivals.

In this scenario, temporal averaging is not an effective solution because if the signal is not equal at every beam shot. Averaging then lowers the signal amplitude and leads to a misleading measurement. Thus, to precisely observe the most relevant beam characteristics, the SNR improvements are needed at the detector level in analog domain.

B. Spatial Averaging with Multichannel Acoustic Sensor

The proposed approach to overcome the temporal average is to use a multichannel acoustic sensor (MAS), composed of N_{ch} different and independent channels. Each channel acquires the same acoustic signal but with a different noise realization from the others. It is therefore possible to carry out a spatial average, mediating the acoustic signal acquired by the various channels to reduce the random noise while maintaining the deterministic signal. Figure 4.4 shows the structure of a linear multichannel sensor, where

in this case 64 different piezoelectrics (channels) are placed side by side to form the sensor.

The main advantage of the spatial average compared to temporal average is that it allows to acquire N_{ch} different signals with a single shot of the beam. Eq. 4.2 shows the SNR increase obtainable with the spatial average, where SNR_{Nch} is the cumulative sensor SNR and SNR_{1Ch} is the single-channel SNR.

$$SNR_{Nch} = SNR_{1Ch} + 10\log_{10} N_{Ch} \qquad \textit{Eq. 4.2}$$

For a sensor with 64 channels, the SNR increase is 18 dB compared to the single channel signal. These performances are very interesting if compared with the time averaging as it allows to obtain the same increase in SNR using 1/64 of the dose.

This result is very promising in terms of dose reduction but requires processing all N_{ch} channels in parallel. The MAS that will be considered in this chapter has 64 channels. Using off-the-shelf components and PCB-implemented electronics to process multichannel sensors is not possible. For example, the space required to build 64 front-ends on a PCB is very large. Considering the size of the ProSD AFE presented in Chapter 2 (10 x 16 cm) and using the same approach for 64 channels, it would result in an extremely bulky sensor going in the opposite direction of miniaturization and portability. Also, there are huge wiring, cross coupling and power consumption difficulties that cannot be solved on PCB. For this reason, MAS require a strong miniaturization of electronics that can only be achieved through an application-specified integrated circuit (ASIC). The next section will show the design of an advanced detector, called High-Resolution Proton Sound Detector (HR-ProSD) that uses a 64-channels MAS and ASIC to increase performance over the state of the art. This detector was designed to validate the proposed multichannel technique and the integrated front-end in sub-clinical 20 MeV scenario, but the same approach can be used for high-energy beams in clinical scenarios. The next section will give an overview of the MAS characteristics and ASIC design.

4.2 High-Resolution Proton Sound Detector (HR-ProSD) Design

Figure 4.5 shows the generic block scheme of the HR-ProSD. It is composed by a Multichannel Acoustic Sensor, an analog front-end ProSD ASIC and a digital signal processing stage (DSP).

The acoustic signal produced by the particle beam propagates to the MAS where it is converted by each channel into voltage domain. Each ProSD ASIC chip has four analog channels which convert the signals of four channels of the MAS and convert them into digital domain. Therefore, 16 ProSD ASICs are sufficient to process the entire MAS in parallel. The digital outputs of the ASICs are acquired by a Field Programmable Gate Array (FPGA), a programmable digital circuit that implements a real-time Bragg Peak localization algorithm. This algorithm exploits the information coming from all 64 channels to increase the SNR by 18 dB and to locate the Bragg Peak in space. Finally, this localization algorithm exploits the difference in the arrival time of the acoustic signal to the various channels to locate the Bragg Peak in 2D and derive the shape of the acoustic source, proportional to the dose deposition in space.

This system is currently in the final development stages. In particular, the acoustic sensor has been fully characterized, the ASIC is in the electrical characterization phase and the DSP on FPGA is in the validation phase. In the coming months, the HR-ProSD will be assembled and (Covid permitting) will be tested by the end of 2020 on a 20 MeV proton beam. This section will give a brief overview of the HR-ProSD and present some preliminary results.

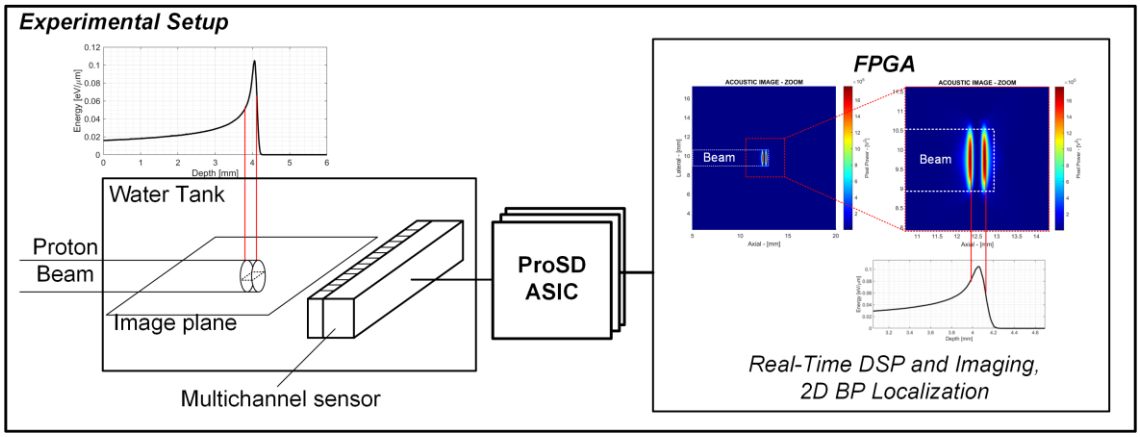

Figure 4.5– HR-ProSD general block scheme

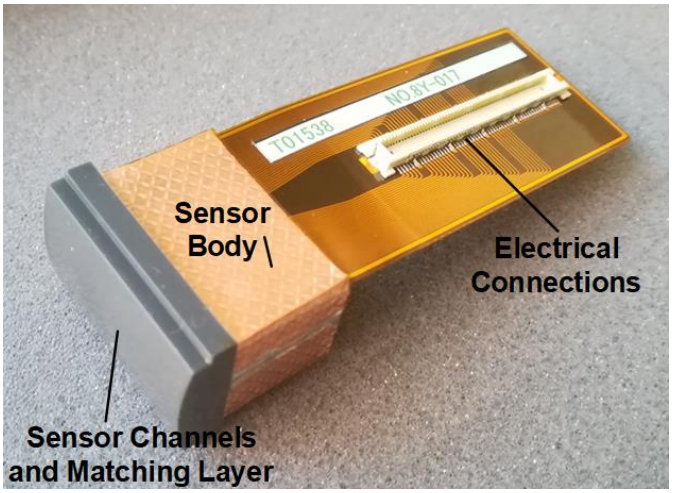

Figure 4.6– NDK multichannel acoustic sensor

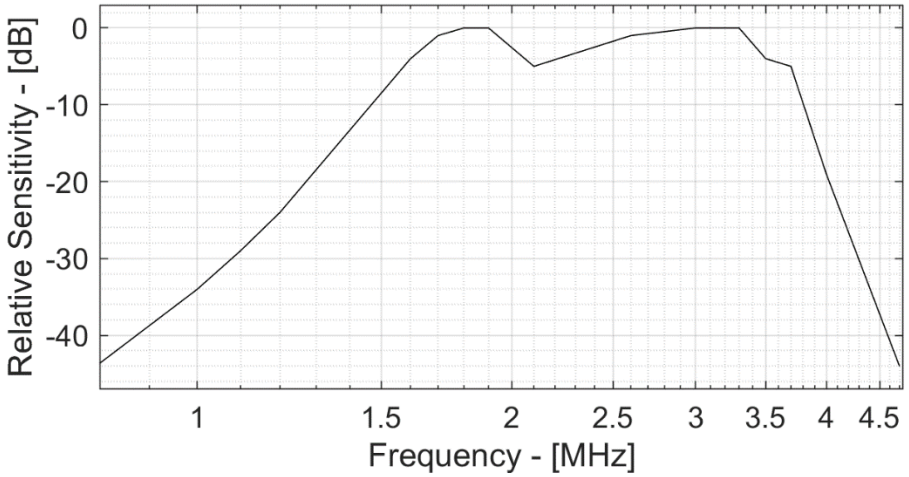

Figure 4.7 – NDK multichannel acoustic sensor frequency response

A. HR-ProSD Multichannel Acoustic Sensor Characterization

In the field of medical ultrasound, there are many high-quality commercial MASs with a suitable bandwidth. The HR-ProSD MAS is a commercial linear array of 64 elements produced by NDK. A picture of the MAS is shown in Figure 4.6. Its frequency response is shown in Figure 4.7. It features a central frequency of 2.5 MHz and an estimated 15 μV/Pa in-band sensitivity. Its 64 channels are 0.3 mm wide and 13 mm long and have a measured capacitance C of 235 pF.

The channel output referred noise power ORN can be estimated equal to $\sqrt{kT/C}$. Thus, each channel ORN power is equal to 4.2 μV_{RMS}. This corresponds to a single-channel IRN power of 323 mPa_{RMS}, obtained dividing the ORN by the sensitivity. However, when all channels are considered together, the total sensor capacitance is 15 nF, corresponding to a total sensor IRN power of 40 mPa_{RMS} (18 dB lower than the single channel IRN). Equivalently, the total sensor IRN can be found by dividing the single channel IRN by $\sqrt{N_{ch}}$ (a factor of 8), exploiting the spatial averaging of multichannel sensor.

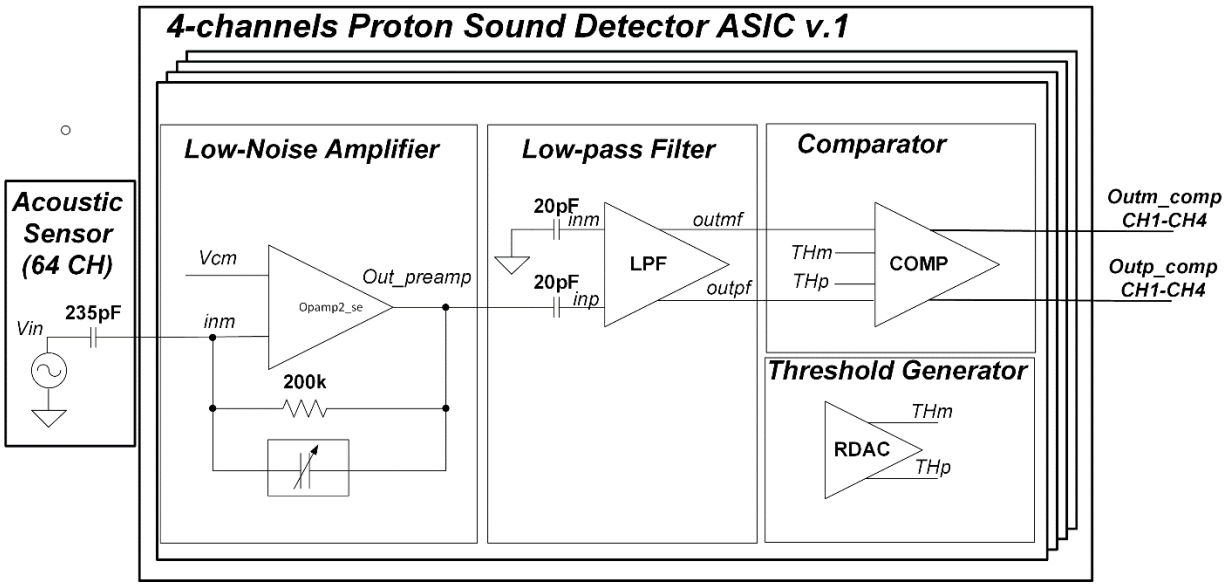

Figure 4.8 – ProSD ASIC Analog Front-End block scheme

B. ProSD ASIC Specifications and Block Scheme

The HR-ProSD ASIC has been developed within the University of Milano - Bicocca Microelectronics group. My contribution in this task was mainly on the system level specification/design, system behavioral validation and part of chip layout, whereas my contribution on the transistor-level design was minimal. Thus, this section will present an overview of the main HR-ProSD analog front-end (AFE) blocks and their simulations in time and frequency domain. The ASIC was implemented in the 28 nm CMOS technology node to increase minimization and exploit the high transconductance efficiency gm/i to reduce power consumption while preserving low-noise performance.

The HR-ProSD ASIC performs three important tasks listed below.

- It amplifies the MAS output signal from few tens of microvolts up in the millivolts range, while preserving the SNR and adapting to the variable input signal amplitude.
- It reduces out-of-band noise power and interferers and adapts to the variable input signal bandwidth.
- It converts the analog signal into digital domain to be processed by a dedicated DSP stage.

To perform these tasks the AFE is composed by three main blocks, as shown in Figure 4.8.

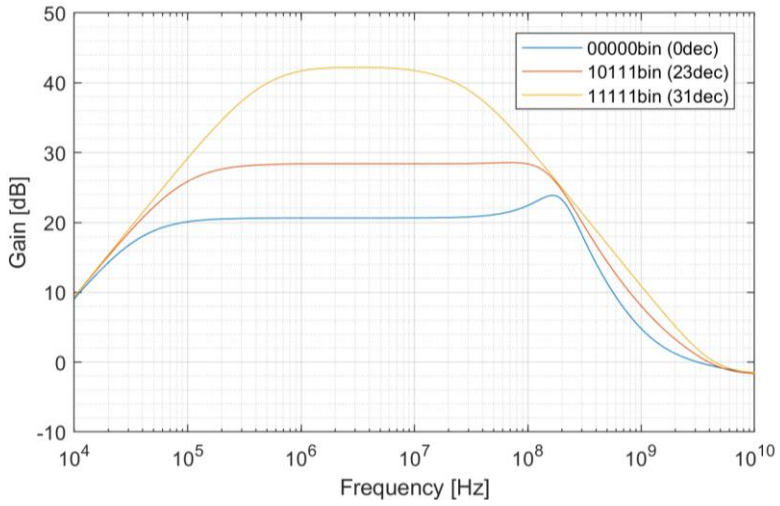

Figure 4.9 – ProSD AFE LNA frequency response with minimum, maximum and nominal gain

Table 3.3 – HR-ProSD Analog Front-End Requirements

LNA Gain (32 steps)	21-42 dB
LPF Gain	21 dB
LPF Bandwidth (16 steps)	2.6 – 6.5 MHz (4.7 MHz Nominal BW)
Variable Threshold Comparator (16 steps)	5 mV – 80 mV (5 mV steps) 80 mV – 160 mV (10 mV steps)
Total AFE Gain	43 – 65 dB

Each block is programmable by a digital signal to adapt to the variability of signals in experimental situations:

- Low-Noise amplifier (LNA): 21-42 dB min/max gain, programmable by a 5-bit word to 32 different values between the min/max values. Its frequency response is shown in Figure 4.9.
- Active low-pass filter (LPF): performs low-pass filtering to reject out-of-band noise power and interferers and to match the frequency response of the ASIC to the signal bandwidth. The bandwidth is programmable by a 4-bit word in the 2.6-6.5 MHz -3 dB frequency (Figure 4.10). Additionally, performs 21 dB amplification, thus leading to a total ProSD AFE gain of 43-65 dB.
- Variable-threshold comparator (VTC): In addition to the analog output of the LPF, ProSD ASIC converts the analog signal into a simple 1-bit signal ready to be processed by the DSP stages. The threshold is programmable (thanks to a DAC threshold generator) by a 4-bit word in the 5 – 80 mV range (5 mV steps) or in the 80-160 mV range (10 mV steps).

The main characteristics of the ProSD AFE are summarized in Table 3.3, whereas the total AFE frequency response (including the acoustic sensor frequency response) is shown in Figure 4.11 for min/max/nominal LNA gain and nominal LPF bandwidth.

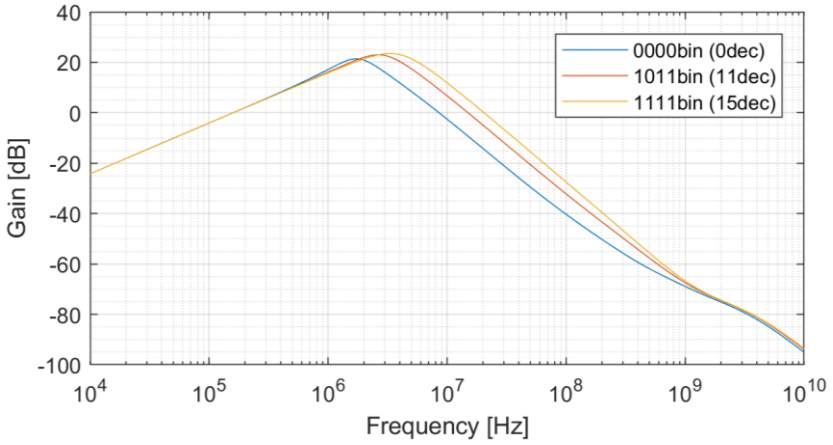

Figure 4.10 – ProSD AFE LPF frequency response with minimum, maximum and nominal bandwidth

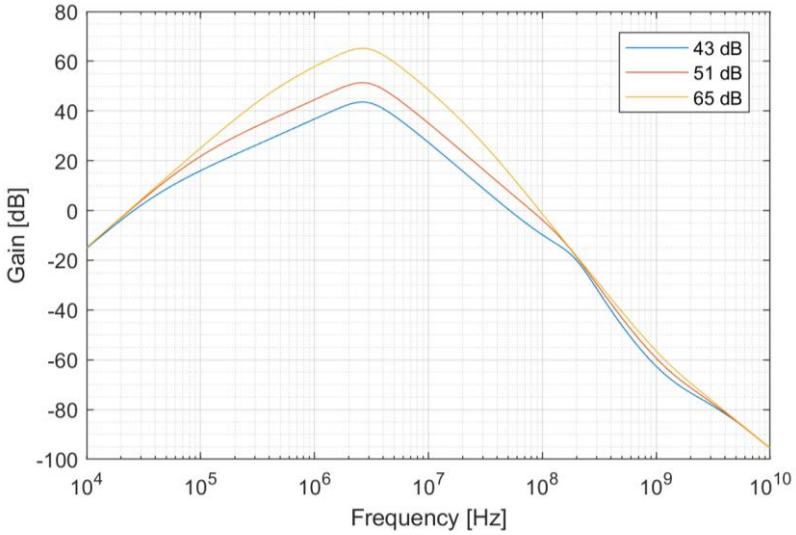

Figure 4.11 – ProSD AFE frequency response with minimum, maximum and nominal gain and nominal bandwidth

C. ProSD ASIC Time Domain Behavioural Simulations

Figure 4.12 shows the transient (left) and transient noise (right) transistor-level simulations of the MAS (single channel) and AFE. A single sinusoidal-like pressure pulse of 6 Pa amplitude is applied to the sensor that produces an output signal with 0.2 $mV_{peak-peak}$ amplitude. This input signal is amplified by the AFE analog stages and the LPF output can be seen with an amplitude of 150 mV_{p-p} (thus the AFE achieves a total 57 dB gain in this scenario). The LNA output signal is phase-shifted compared to the AS output by the AFE frequency response. This behavior is expected in analog circuits but could lead to a systematic error in measuring the acoustic wave Time of Flight. However, since the transfer function (and thus phase delay and signal group delay) are well characterized, this systematic error can be easily compensated, along with the MAS channels delays.

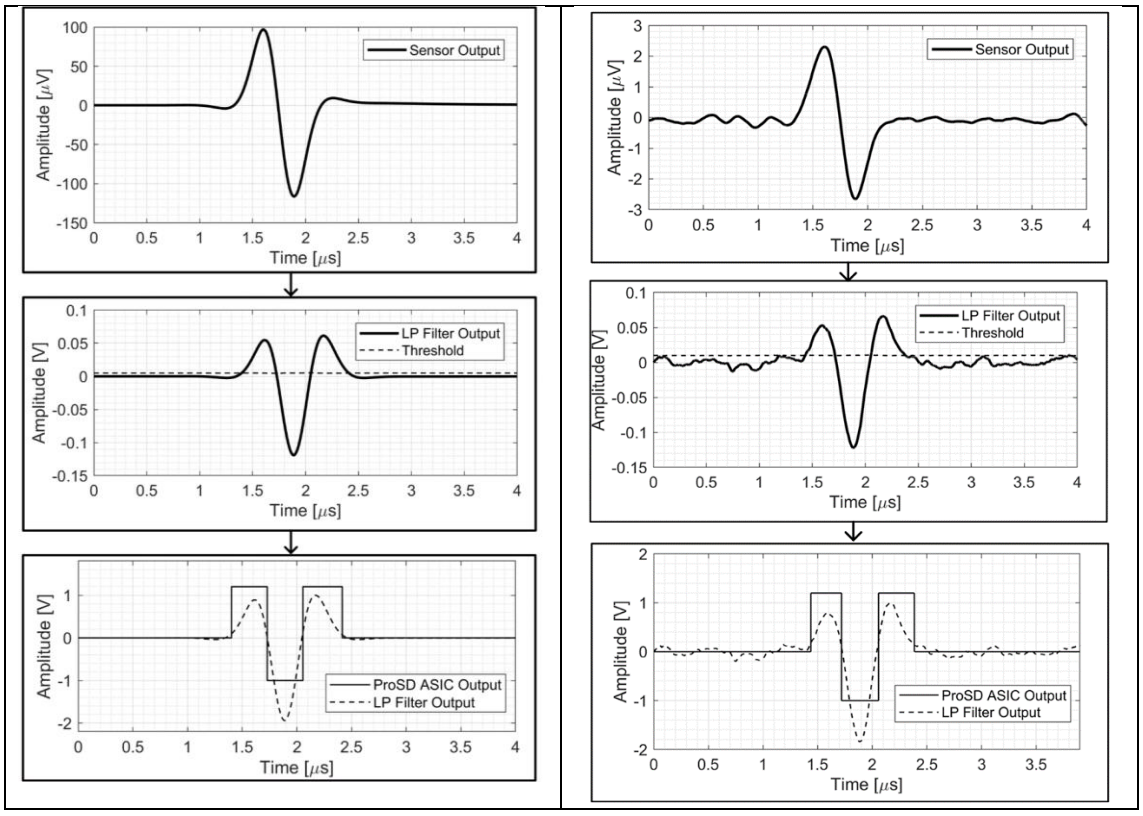

Figure 4.12 – Transient (left) and transient noise (right) simulations of the ProSD AFE

Finally, the comparator allows to reconstruct the signal shape and easily measure the time of flight of the acoustic wave. The 64 channels independently measured times of flight allow to precisely localize the BP in space. Transient noise simulation adds AS and AFE noise considering all noise sources inside the AFE (resistors and transistors). The SNR at the AS output is equal to 24.5 dB, considering 100 $\mu V_{0\text{-peak}}$ signal amplitude and 4.2 μV_{RMS} AS noise power. The AFE input referred noise power is 2.2 μV_{RMS}, thus leading to a total 4.7 μV_{RMS} input referred noise power and an AFE output SNR equal to 23.5 dB. Thus, the AFE achieves a Noise Figure equal to 1 dB.

D. HR-ProSD ASIC Layout

To enhance the system miniaturization, four channels of the ProSD AFE have been layout into a single silicon die of 1x1 mm area including pads. The channels are oriented vertically, with the inputs at the bottom in Figure 4.13 and the digital outputs at the top. In each channel are visible, from bottom to top, the LNA and the capacitive array that implements the variable gain, the LPF and its programmable capabilities, the comparator with the DAC and the output buffers. In the upper part of the channels there are also polarization circuits and comparators output buffers that drive the capacitive load external to the chip (namely, the FPGA input pins). Finally, a 14*4 bit SIPO shift register stores the bits that independently program each channel's LNA, LPF and VTC.

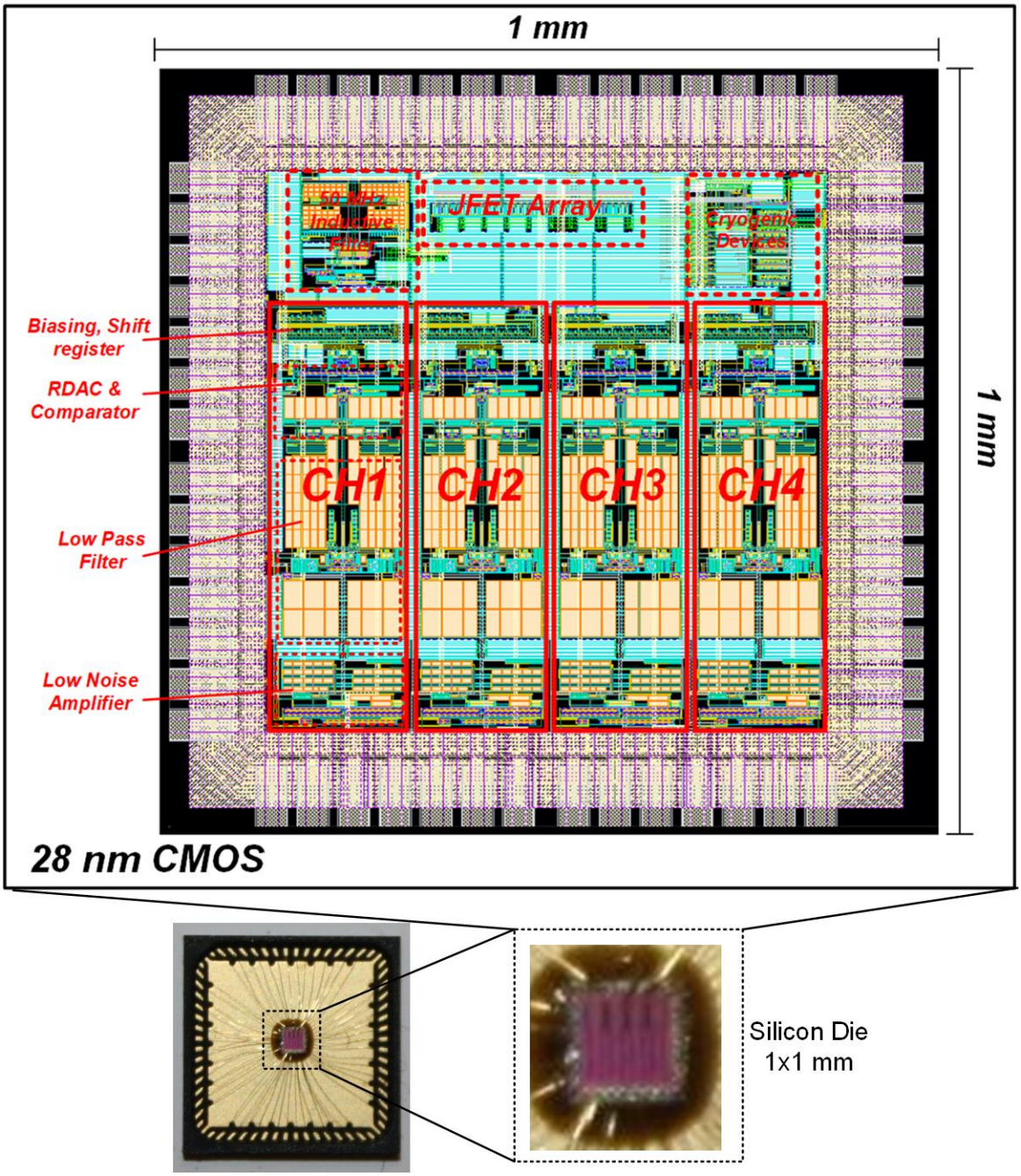

Figure 4.13 – ProSD ASIC layout scheme and die picture

The digital signals (data and clock) enter the chip from the left, runs through the shift register to the right and can be monitored by a pin on the right of the chip to verify the correct programming of the stages. Finally, the top of the chip contains additional circuits not related to the ProSD AFE to efficiently exploit the remaining die area. A picture of the silicon chip inside the packaging and a close-up of the silicon die can be seen in Figure 4.13 – bottom.

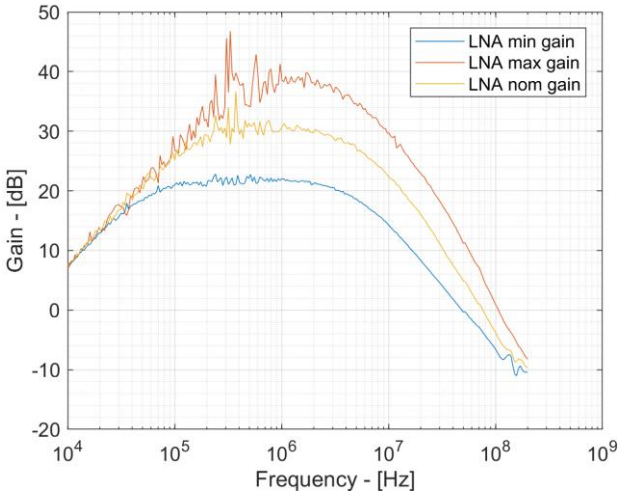

Figure 4.14 – Preliminary measure of the ProSD ASIC LNA frequency response

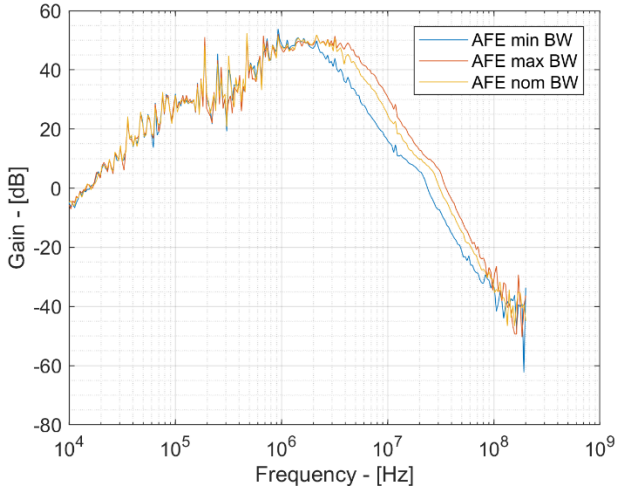

Figure 4.15 – Preliminary measure of the ProSD ASIC AFE frequency response

E. Preliminary ASIC Electrical Validation

A preliminary measurement of the frequency response shows that the chip is indeed "alive", but a complete and precise characterization of the AFE will be done in the next months. From the frequency response of the LNA (Figure 4.14) it is possible to observe the 22 dB of minimum gain as expected, while the maximum measured gain is slightly lower. This gain difference is likely due to signal compression. In fact, to observe a noise-free frequency response, it is necessary to use a sufficiently powerful input signal to the AFE. However, given the high gain of the LNA, in this way there is the risk of saturating or compressing the signal, thus observing a decrease in gain. This aspect will be improved in the future electrical characterization of the chip. Figure 4.15 shows the frequency response of the entire channel. Again, there is a tradeoff between the presence of noise in the measurement and the compression of the signal due to the high gain of the front end.

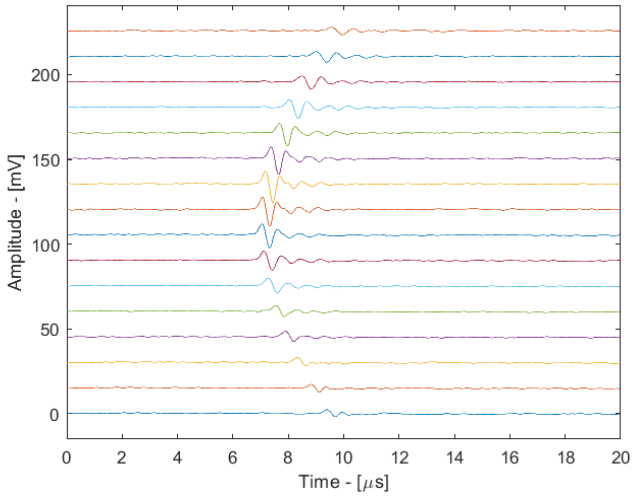

Figure 4.16 – Acoustic signal from a point-like source acquired by the HR-ProSD MAS

Finally, the measured current consumption of the 4-channels AFE is 25 mA at 1.2 V power supply, equal to 30 mW total power consumption or 7.5 mW/channel.

F. Digital Signal Processing Stages

Finally, this section will give a brief introduction to the DSP stages that have been developed for the HR-ProSD. At present, these stages have been tested with simulated signals from the iono-LTI system described in Chapter 3 and from acoustic signals (Figure 4.16) acquired through a photoacoustic testbench described in [39] and a PCB front-end.

As already mentioned, the use of a MAS, in addition to bringing the advantage of increasing SNR through spatial averaging, allows to locate the Bragg peak in a 2D space and to obtain an acoustic image of the source proportional to the pressure distribution.

By applying a simple beamforming algorithm on FPGA, a real-time localization/imaging system of the Bragg peak was obtained. Thanks to the hardware implementation, this system allows to generate acoustic images at 256x256 pixels with 7 ms of latency, corresponding to> 100 frames per second. The system was first modeled in Matlab using simulated and measured signals from the MAS. The result is shown in Figure 4.17, where the qualitative image of an acoustic source of 1 mm in diameter and 300 μm thick (comparable to the size of the Bragg peak at 20 MeV) is generated starting from the acoustic signals. Finally, Figure 4.18 shows two acoustic images generated using the 64 single-bit outputs of the HR-ProSD AFE obtained from Cadence simulations using real acoustic signals acquired by the MAS. This gives a qualitative perspective on the final performance and behavior of the HR-ProSD.

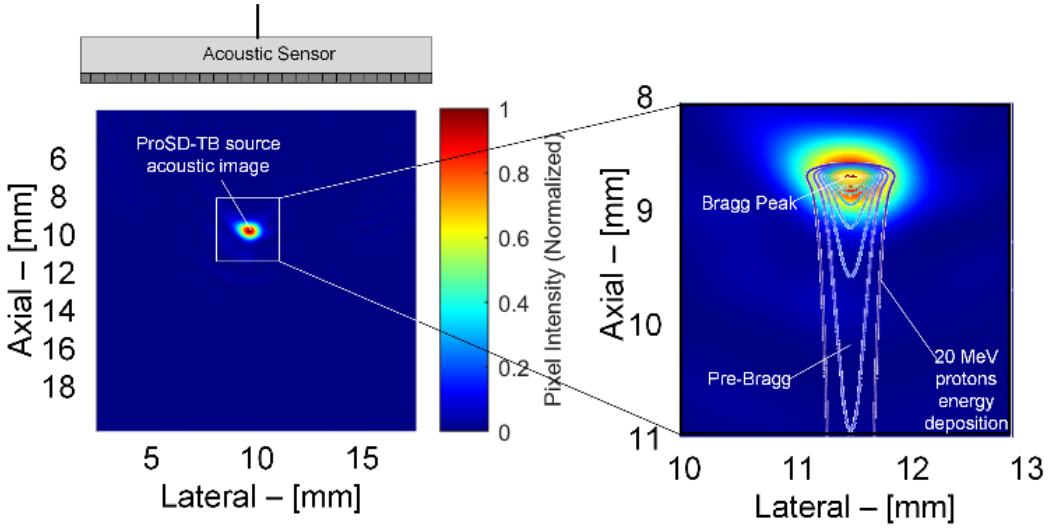

Figure 4.17 – Preliminary results of the HR-ProSD DSP

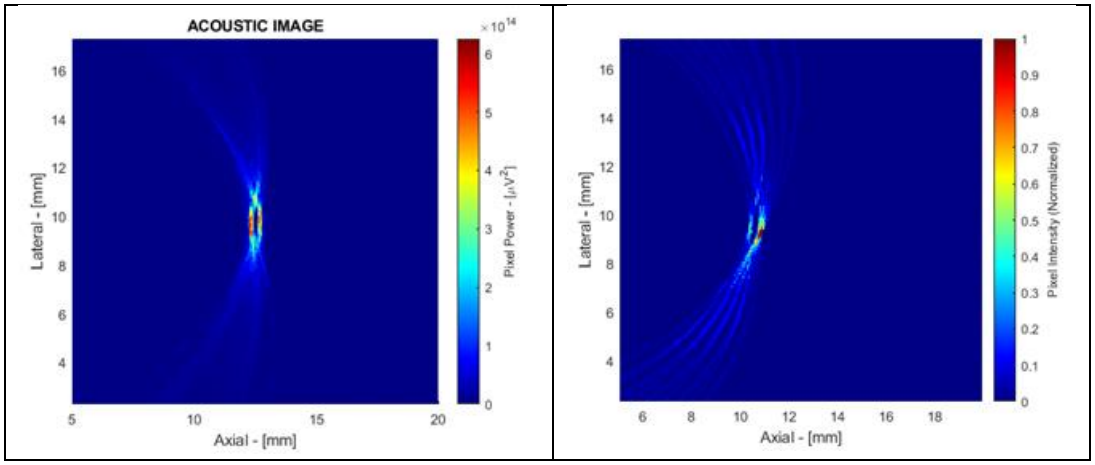

Figure 4.18 – Preliminary results of the HR-ProSD DSP – 64x 1-bit signals

However, a complete and quantitative characterization of the whole system is needed to precisely determine its performance in experimental conditions.

Conclusions

In this work the design and characterization of dedicated ionacoustic detectors were presented, which aim to improve the accuracy in determining the range of particle beams in water absorbers. It has been shown how the state of the art uses general purpose detectors and makes use of hand-made measurements, and how this aspect strongly limits the results obtained with clinical energy beams. In particular, it has been shown that the massive use of post-processing is not an effective way to increase the signal-to-noise ratio (SNR), as it involves an additional dose not compatible with clinical treatments. For this reason, the improvement of SNR must be achieved at the detector level in the analog domain. In Chapter 2 it was shown how to add dedicated electronics to a general-purpose detector improves the SNR by a factor of 6 dB, allowing to obtain a better precision for the same dose, or a reduction in the dose necessary to obtain a given precision. equal to a factor of 4 compared to the general-purpose detector. Subsequently, a simple model was developed that exploits the properties of linear time invariant systems to derive the ionoacoustic signal in the different experimental scenarios. This simplified but accurate model was validated by comparing the signals produced with those measured in an experimental setting. Finally, it was used to show how clinical scenarios are critical from the SNR point of view. It was therefore shown that time-domain averaging does not allow to observe signals in the clinical setting and instead a solution based on space-domain averaging has been proposed. This solution uses multi-channel sensors to increase SNR by a factor of 18 dB compared to single channel sensors at the same dose. We have shown how this approach requires integrated electronics and signal processing implemented in hardware. Finally, the preliminary characterization of a High-Resolution Proton Sound Detector (HR-ProSD) was shown which allows to reduce the dose required to obtain a certain precision by a factor of 64 compared to a single channel detector in 20 MeV pre-clinical scenarios.

References

[1] Ohno, T. (2013). Particle radiotherapy with carbon ion beams. EPMA Journal, 4(1), 9.

[2] L. Sulak *et al.*, “Experimental studies of the acoustic signature of proton beams traversing fluid media,” *Nucl. Instrum. Methods*, vol. 161, no. 2, pp. 203–217, 1979.

[3] Y. Hayakawa *et al.*, “Acoustic pulse generated in a patient during treatment by pulsed proton radiation beam,” *Radiat. Oncol. Investigations*, vol. 3, no. 1, pp. 42–45, 1995.

[4] W. Assmann, S. Kellnberger, S. Reinhardt, et al., “Ionoacoustic characterization of the proton Bragg peak with sub-millimeter accuracy,” *Medical Physics*, Vol. 42, no. 2, pp. 567-574, Feb 2015.

[5] Patch, S. K., et al. "Thermoacoustic range verification using a clinical ultrasound array provides perfectly co-registered overlay of the Bragg peak onto an ultrasound image." Physics in Medicine & Biology 61.15 (2016): 5621.

[6] Jones, Kevin C., et al. "Acoustic time-of-flight for proton range verification in water." Medical physics 43.9 (2016): 5213-5224.

[7] Assmann, W., et al. "Ionoacoustic characterization of the proton Bragg peak with submillimeter accuracy." Medical physics 42.2 (2015): 567-574.

[8] Geng, Changran, et al. "Physical parameter optimization scheme for radiobiological studies of charged particle therapy." Physica Medica 51 (2018): 13-21.

[9] Ghithan, Sharif, et al. "Development of a PET cyclotron based irradiation setup for proton radiobiology." Journal of Instrumentation 10.02 (2015): P02010.

[10] Vallicelli, E. A., et al. "22 dB Signal-to-Noise Ratio Real-Time Proton Sound Detector for Experimental Beam Range Verification." Transaction on Circuits and Systems I: Regular Papers (2020)

[11] Dosanjh, Manjit, et al. "Medical Applications at CERN and the ENLIGHT Network." Frontiers in oncology 6 (2016).

[12] Knoll, Glenn F. Radiation detection and measurement. John Wiley & Sons, 2010.

[13] Y. Jongen. “The medical applications of cyclotrons”. CAS Bruges, June 23rd 2009.

[14] K. Parodi, et al. “Patient study of in vivo verification of beam delivery and range, using positron emission tomography and computed tomography imaging after proton therapy”. Int. J. Radiat. Oncol., Biol., Phys. 68, 920–934 (2007).

[15] C. H. Min, C. H. Kim, M. Y. Youn, and J. W. Kim, “Prompt gamma measurements for locating the dose falloff region in the proton therapy”. Appl. Phys. Lett. 89, 183517 (2006).

[16] Knopf, Antje-Christin, and Antony Lomax. "In vivo proton range verification: a review." Physics in medicine and biology 58.15 (2013): R131.

[17] Wang, Lihong V. "Tutorial on photoacoustic microscopy and computed tomography." IEEE Journal of Selected Topics in Quantum Electronics 14.1 (2008): 171-179.

[18] De Bonis, G. "Acoustic signals from proton beam interaction in water—Comparing experimental data and Monte Carlo simulation." Nuclear Instruments and Methods in Physics Research Section A: Accelerators, Spectrometers, Detectors and Associated Equipment 604.1 (2009): S199-S202.

[19] Riva, Michele, et al. "Acoustic Analog Front End for Proton Range Detection in Hadron Therapy." IEEE transactions on biomedical circuits and systems 12.4 (2018): 954-962.

[20] S. Agostinelli, et al. “Geant4-a simulation toolkit,” Nucl. Instrum. Methods Phys. Res., Sect. A 506, 250–303 (2003).

[21] B. E. Treeby and B. T. Cox, “k-Wave: MATLAB toolbox for the simulationand reconstruction of photoacoustic wave fields,” J. Biomed. Opt. 15, 021314 (2010).

[22] Jones, Kevin C., et al. "How proton pulse characteristics influence protoacoustic determination of proton-beam range: simulation studies." Physics in medicine and biology 61.6 (2016): 2213.

[23] Jones, K. C., et al. "Proton beam characterization by proton-induced acoustic emission: simulation studies." Physics in medicine and biology 59.21 (2014): 6549.

[24] G. A. Askariyan, B. A. Dolgoshein, A. N. Kalinovsky, and N. V. Mokhov, “Acoustic detection of high energy particle showers in water”. Nucl. Instrum. Methods 164, 267–278 (1979).

[25] Ahmad, Moiz, et al. "Theoretical detection threshold of the proton-acoustic range verification technique." Medical physics 42.10 (2015): 5735-5744.

[26] Kipergil, Esra Aytac, et al. "An analysis of beam parameters on proton-acoustic waves through an analytic approach." Physics in Medicine and Biology 62.12 (2017): 4694.

[27] Kellnberger, Stephan, et al. "Ionoacoustic tomography of the proton Bragg peak in combination with ultrasound and optoacoustic imaging." Scientific reports 6 (2016).

[28] Lehrack, S., et al. "Range Verification with Ionoacoustics: simulations and measurements at a clinical proton synchro-cyclotron." Radiotherapy and Oncology 118 (2016): S66-S67.

[29] Jones, Kevin C., et al. "Experimental observation of acoustic emissions generated by a pulsed proton beam from a hospital-based clinical cyclotron." Medical physics 42.12 (2015): 7090-7097.

[30] Chen, Chen-Tung, and Frank J. Millero. "Speed of sound in seawater at high pressures." The Journal of the Acoustical Society of America 62.5 (1977): 1129-1135.

[31] M. De Matteis, et al. "A 0.13 µm-CMOS 90µW 51dB-SNR continuous-time accelerometer front-end with 10b SAR-ADC." SENSORS, 2015 IEEE. IEEE, 2015.

[32] M. De Matteis, et al. "A 0.13 μm-CMOS 90μW 51dB-SNR continuous-time accelerometer front-end with 10b SAR-ADC." Analog Integrated Circuits and Signal Processing. Volume 92, Number 2, 2017, Page(s): 1 – 11.

[33] https://ese.wustl.edu/ContentFiles/Research/UndergraduateResearch/CompletedProjects/WebPages/sp09/JoshuaYork/avs.html

[34] Shipps, J. Clay, and Bruce M. Abraham. "The use of vector sensors for underwater port and waterway security." Sensors for Industry Conference, 2004. Proceedings the ISA/IEEE. IEEE, 2004.

[35] Shipps, J. Clay, and Ken Deng. "A miniature vector sensor for line array applications." OCEANS 2003. Proceedings. Vol. 5. IEEE, 2003.

[36] Silvia, Manuel T., and Roger T. Richards. "A theoretical and experimental investigation of low-frequency acoustic vector sensors." OCEANS'02 MTS/IEEE. Vol. 3. IEEE, 2002.

[37] Mirandola, Alfredo, et al. "Dosimetric commissioning and quality assurance of scanned ion beams at the Italian National Center for Oncological Hadrontherapy." Medical physics 42.9 (2015): 5287-5300.

[38] M. Pelgrom, et al. "Matching properties of MOS transistors." IEEE Journal of solid-state circuits 24.5 (1989): 1433-1439.

[39] Vallicelli, Elia A., et al. "Photoacoustic Sensing Instrumentation using 70 W 905 nm Pulsed Laser Source for Proton-Induced Thermoacoustic Effect Emulation." 2020 IEEE Sensors. IEEE, 2020.

Publications

Invited Journal Publications

- Vallicelli, E. A., Baschirotto, A., Lehrack, S., ... & De Matteis, M. 22 dB Signal-to-Noise-Ratio Real-Time Proton Sound Detector for Experimental Beam Range Verification. IEEE Transactions on Circuits and Systems I

- Vallicelli, E. A., Turossi, D., Gelmi, L., & De Matteis, M. A 0.3nV/√Hz Input-Referred-Noise Analog Front End for Radiation-Induced Thermo-Acoustic Pulses. Integration: The VLSI Journal.

Journal Publications

- Vallicelli, E. A., Reato, M., Maschietto, M., Vassanelli, S., Guarrera, D., Rocchi, F., ... & De Matteis, M. (2018). Neural Spike Digital Detector on FPGA. Electronics, 7(12), 392.

- Ardid, M., Baschirotto, A., Burgio, N., Corcione, M., Cretara, L., De Matteis, M., ... & Santagata, A. (2019). Effects of the thermodynamic conditions on the acoustic signature of bubble nucleation in superheated liquids used in dark matter search experiments. The European Physical Journal C, 79(11), 961.

- Riva, M., Vallicelli, E. A., Baschirotto, A., & De Matteis, M. (2018). Acoustic Analog Front End for Proton Range Detection in Hadron Therapy. IEEE transactions on biomedical circuits and systems, 12(4), 954-962.

- De Matteis, M., De Blasi, M., Vallicelli, E. A., Zannoni, M., Gervasi, M., Bau, A., ... & Baschirotto, A. (2017). A CMOS application-specified-integrated-circuit for 40 GHz high-electron-mobility-transistors automatic biasing. Review of Scientific Instruments, 88(2), 024702.

Conference Contributions – Speaker

- Vallicelli, E. A., Gelmi, L., Bertoni, R., Fulgione, W., Tambaro, M., Baschirotto, A., & De Matteis, M. (2019, July). A 0.3 nV/√ Hz Input-Referred-Noise Analog Front-End for Weakly-Interacting-Massive-Particles (WIMPs) Acoustic Sensing in Bubbles-Chamber Detectors. In 2019 15th Conference on Ph. D Research in Microelectronics and Electronics (PRIME) (pp. 197-200). IEEE. **Gold leaf award – best 10% paper**.

- Tambaro, M., Vallicelli, E. A., Tomasella, D., Baschirotto, A., Vassanelli, S., Maschietto, M., & De Matteis, M. (2019, July). Real-Time Neural (RT-Neu) Spikes Imaging by a 9375 sample/(sec pixel) 32× 32 pixels Electrolyte-Oxide-Semiconductor Biosensor. In 2019 15th Conference on Ph. D Research in Microelectronics and Electronics (PRIME) (pp. 233-236). IEEE. **Bronze leaf award – best 30% paper**

- Vallicelli, E. A., Baschirotto, A., Lehrack, S., & De Matteis, M. (2019). Mixed-Signal Ionoacoustic Analog Front-End for Proton Range Verification with 24 µm Precision at 0.8 Gy Bragg Peak Dose. In 2019 International Conference on Electronics Circuits and Systems (ICECS). IEEE.

- Vallicelli, E. A., Baschirotto, A., De Matteis, M. (2019). 10 MHz -3 dB Bandwidth 360 µW Power SourceFollower Low-Pass Filter for Multi-Channel Acoustic Analog Front-End in CMOS 0.18 µm. In 2019 International Conference on Electronics Circuits and Systems (ICECS). IEEE.

- Riva, M., Vallicelli, E. A., Baschirotto, A., & De Matteis, M. (2019). Modeling the Acoustic Field Generated by a Pulsed Beam for Experimental Proton Range Verification. In EPJ Web of Conferences (Vol. 216, p.03005). EDP Sciences.

- Vallicelli, E. A., Riva, M., Zannoni, M., Baschirotto, A., & De Matteis, M. (2019). Analog and Digital Signal Processing for Pressure Source Imaging at 190 MeV Proton Beam. In EPJ Web of Conferences (Vol. 216, p. 04003). EDP Sciences.

Conference Contribution – Poster

- Riva, M., Vallicelli, E., Baschirotto, A., & De Matteis, M. (2017, October). Acoustic analog front-end for Bragg-peak detection in hadron therapy. In 2017 IEEE Biomedical Circuits and Systems Conference (BioCAS) (pp. 1-4). IEEE.

- Vallicelli, E. A., De Matteis, M., Baschirotto, A., Rescati, M., Reato, M., Maschietto, M., ... & Zeiter, R. (2017, October). Neural spikes digital detector/sorting on FPGA. In 2017 IEEE Biomedical Circuits and Systems Conference (BioCAS) (pp. 1-4). IEEE.

Other Conference Contributions

- Vallicelli, E. A., Fary, F., Baschirotto, A., De Matteis, M., Reato, M., Maschietto, M., ... & Zeitler, R. (2018, June). Real-time digital implementation of a principal component analysis algorithm for neurons spike detection. In 2018 International Conference on IC Design & Technology (ICICDT) (pp. 33-36). IEEE.

- Fary, F., Mangiagalli, L., Vallicelli, E., De Matteis, M., & Baschirotto, A. (2019, September). A 28nm bulkCMOS 50MHz 18 dBm-IIP3 Active-RC Analog Filter based on 7 GHz UGB OTA. In ESSCIRC 2019-IEEE 45th European Solid State Circuits Conference (ESSCIRC) (pp. 253-256). IEEE.

- Fary, F., Vallicelli, E. A., De Matteis, M., & Baschirotto, A. (2018, June). About figure-of-merit for continuous-time analog filters. In 2018 International Conference on IC Design & Technology (ICICDT) (pp. 57-60). IEEE.

.

.